Supercooled liquid water clouds observed over Dome C, Antarctica: temperature sensitivity and surface radiation impact

Philippe Ricaud[1], Massimo Del Guasta[2], Angelo Lupi[3], Romain Roehrig[1], Eric Bazile[1], Pierre Durand[4], Jean-Luc Attié[4], Alessia Nicosia[3] and Paolo Grigioni[5]

[1]CNRM, Université de Toulouse, Météo-France, CNRS, Toulouse, France (philippe.ricaud@meteo.fr; romain.roehrig@meteo.fr; eric.bazile@meteo.fr)

[2]INO-CNR, Sesto Fiorentino, Italy (massimo.delguasta@ino.cnr.it)

[3]ISAC-CNR, Bologna, Italy (a.lupi@isac.cnr.it; a.nicosia@isac.cnr.it)

[4]Laboratoire d'Aérologie, Université de Toulouse, CNRS, UPS, Toulouse, France (pierre.durand@aero.obs-mip.fr; jean-luc.attie@aero.obs-mip.fr)

[5]ENEA, Roma, Italy (paolo.grigioni@enea.it)

Correspondence: philippe.ricaud@meteo.fr

14 December 2022, Version REV01 V01

Submitted to **Atmospheric Chemistry and Physics**

23   **Abstract**

24   Clouds affect the Earth climate with an impact that depends on the cloud nature (solid/

25   liquid water). Although the Antarctic climate is changing rapidly, cloud observations are sparse

26   over Antarctica due to few ground stations and satellite observations. The Concordia station is

27   located on the East Antarctic Plateau (75°S, 123°E, 3233 m above mean sea level), one of the

28   driest and coldest places on Earth. We used observations of clouds, temperature, liquid water

29   and surface radiation performed at Concordia during 4 austral summers (December 2018-2021)

30   to analyse the link between liquid water and temperature and its impact on surface radiation in

31   the presence of supercooled liquid water (liquid water for temperature less than 0°C) clouds

32   (SLWCs). Our study has shown that, at the Concordia station, the very local structure of the ice

33   surface highly impacts the surface albedo and therefore the radiation budget. The ERA5 or

34   CERES data are not able to reproduce the diurnal variation of the local albedo. We established

35   that a two-sine empirical function with 24-h and 12-h periods well fits the BSRN observed

36   albedo. We show that ground-based observations are likely the best way to estimate the Net SR

37   in Concordia. Our analysis shows that, within SLWCs, temperature logarithmically increases

38   from -36.0°C to -16.0°C when liquid water path increases from 1.0 to 14.0 g m^{-2}, and SLWCs

39   positively impact the net surface radiation, which logarithmically increases by 0.0 to 50.0 W m^{-}

40   ^{2} when liquid water path increases from 1.7 to 3.0 g m^{-2}. We finally estimate that SLWCs have

41   a great potential radiative impact over Antarctica whatever the season considered, up to 5.0 W

42   m^{-2} over the Eastern Antarctic Plateau and up to 30 W m^{-2} over the Antarctic Peninsula in

43   summer.

1. Introduction

Antarctic clouds play an important role in the climate system by influencing the Earth's radiation balance, both directly at high southern latitudes and, indirectly, at the global level through complex teleconnections (Lubin et al., 1998). However, in Antarctica, ground stations are mainly located on the coast and yearlong observations of clouds and associated meteorological parameters are scarce. Meteorological analyses and satellite observations of clouds can nevertheless give some information on cloud properties suggesting that clouds vary geographically, with a fractional cloud cover ranging from about 50 to 60% around the South Pole to 80-90% near the coast (Bromwich et al., 2012; Listowski et al., 2019). In situ aircraft measurements performed mainly over the Western Antarctic Peninsula (Grosvenor et al., 2012; Lachlan-Cope et al., 2016) and nearby coastal areas (O'Shea et al., 2017) provided new insights to polar cloud modelling and highlighted sea-ice production of Cloud-Condensation Nuclei and Ice Nucleating Particles (see e.g. Legrand et al., 2016). Mixed-phase clouds (made of solid and liquid water) are preferably observed near the coast (Listowski et al., 2019) with larger ice crystals and water droplets (Lachlan-Cope, 2010; Lachlan-Cope et al., 2016; Grosvenor et al., 2012; O'Shea et al., 2017; Grazioli et al., 2017). Based on the raDAR/liDAR-MASK (DARDAR) spaceborne products (Listowski et al., 2019), it has been found that clouds are mainly constituted of ice above the continent. The abundance of Supercooled Liquid Water (SLW, the water staying in liquid phase below 0°C) clouds depends on temperature and liquid/ice fraction. It decreases sharply poleward, and is two to three times lower over the Eastern Antarctic Plateau than over the Western Antarctic. An important point remains the inability of both research and operational weather prediction models to accurately represent the clouds (especially SLW clouds, SLWCs) in Antarctica causing biases of several tens W m^{-2} on net surface radiation (Listowski and Lachlan-Cope, 2017; King et al., 2006, 2015; Bromwich et al., 2013) over and beyond the Antarctic (Lawson and Gettelman, 2014; Young et al. 2019).

70 From year-long LIDAR observations of mixed-phase clouds at South Pole (Lawson and

71 Gettelman, 2014), SLWCs were shown to occur more frequently than in earlier aircraft

72 observations or weather model simulations, leading to biases in the surface radiation budget

73 estimates.

74   Liquid water in clouds may occur in supercooled form due to a relative lack of ice nuclei

75 for temperature greater than -39°C and less than 0°C. Very little SLW is then expected because

76 the ice crystals that form in this temperature range will grow at the expense of liquid droplets

77 (called the "Wegener-Bergeron-Findeisen" process; Wegener, 1911; Bergeron, 1928;

78 Findeisen, 1938; Storelvmo and Tan, 2015). Nevertheless, SLW is often observed at negative

79 temperatures higher than -20°C at all latitudes being a danger to aircraft since icing on the wings

80 and airframe can occur, reducing lift, and increasing drag and weight. As temperature decreases

81 to -36°C, SLW dramatically lessens, so it is highly difficult 1) to observe SLWCs and 2) to

82 quantify the amount of liquid water present in SLWCs. But during the Year Of Polar Prediction

83 (YOPP) international campaign, recent observations performed at the Dome C station in

84 Antarctica of 2 case studies in December 2018 have revealed SLWCs with temperature between

85 -20°C and -30°C and Liquid Water Path (LWP, the liquid water content integrated along the

86 vertical) between 2 to 20 g m^{-2}, as well as a considerable impact on the net Surface Radiation

87 (SR) that exceeded the simulated values by 20-50 W m^{-2} (Ricaud et al., 2020).

88   The Dome C (Concordia) station, jointly operated by French and Italian institutions in the

89 Eastern Antarctic Plateau (75°06'S, 123°21'E, 3233 m above mean sea level, amsl), is one of

90 the driest and coldest places on Earth with surface temperatures ranging from about -20°C in

91 summer to -70°C in winter. There are three main instruments relevant to this study that have

92 been routinely running for about 10 years: 1) The H$_2$O Antarctica Microwave Stratospheric and

93 Tropospheric Radiometer (HAMSTRAD, Ricaud et al., 2010a) to obtain vertical profiles of

94 temperature and water vapour, as well as the LWP. 2) The tropospheric depolarization LIDAR

95 (Tomasi et al., 2015) to obtain vertical profiles of backscatter and depolarization to be used for

96 the detection of SLWCs. 3) The Baseline Surface Radiation Network (BSRN) station to

97 measure surface longwave (4–50 μm) and shortwave (0.3–3 μm), downward and upward

98 surface radiation (SR) from which the Net SR, calculated as the difference between the

99 downward and upward SRs, can be computed (Driemel et al., 2018) as:

100 $$Net = LWD - LWU + SWD - SWU \qquad (1)$$

101 where LWD, LWU, SWD and SWU correspond to Longwave Downward, Longwave Upward,

102 Shortwave Downward and Shortwave Upward SRs, respectively. Hereafter, we will use either

103 the term "radiative flux" or "radiation", the latter consistent with the terminology presented

104 page 256 by Stull (1988).

105 The article is structured as follows. Section 2 presents the instruments during the period of

106 study. In section 3, we detail the methodology employed to detect the SLWCs and calculate

107 their impact on SR, and we present the statistical method to emphasize the relationship between

108 temperature and LWP on one hand, and SR and LWP on the other hand. The results are

109 highlighted in section 4 and discussed in section 5, before concluding in section 6.

110

111 **2. Instruments**

112 We have used the observations from 3 instruments held at the Dome C station, namely the

113 LIDAR instrument to classify the cloud as SLWC, the HAMSTRAD microwave radiometer to

114 obtain LWP and vertical profile of temperature, and the BSRN network to measure the SR

115 components: LWD, LWU, SWD and SWU to finally obtain the Net SR.

116 *2.1. LIDAR*

117 The tropospheric depolarization LIDAR (532 nm) has been operating at Dome C since 2008

118 (see http://lidarmax.altervista.org/englidar/_Antarctic%20LIDAR.php). The LIDAR provides

119 5-min tropospheric profiles of clouds characteristics continuously, from 20 to 7000 m above

120 ground level (agl), with a resolution of 7.5 m. For the present study, the most relevant parameter

121 is the LIDAR depolarization ratio (Mishchenko et al., 2000) that is a robust indicator of non-

122 spherical shape for randomly oriented cloud particles. A depolarization ratio below 10% is

123 characteristic of SLWC, while higher values are produced by ice particles. The possible

124 ambiguity between SLW droplets and oriented ice plates is avoided at Dome C by operating

125 the LIDAR 4° off-zenith (Hogan and Illingworth, 2003).

126 *2.2. HAMSTRAD*

127 HAMSTRAD is a microwave radiometer that profiles water vapour, liquid water and

128 tropospheric temperature above Dome C. Measuring at both 60 GHz (oxygen molecule line

129 (O_2) to deduce the temperature) and 183 GHz (H_2O line), this unique, state-of-the-art

130 radiometer was installed on site for the first time in January 2009 (Ricaud et al., 2010a and b).

131 The measurements of the HAMSTRAD radiometer allow the retrieval of the vertical profiles

132 of water vapour and temperature from the ground to 10-km altitude with vertical resolutions of

133 30 to 50 m in the Planetary Boundary Layer (PBL), 100 m in the lower free troposphere and

134 500 m in the upper troposphere-lower stratosphere. The time resolution is adjustable and fixed

135 at 60 seconds since 2018. Note that an automated internal calibration is performed every 12

136 atmospheric observations and lasts about 4 minutes. Consequently, the atmospheric time

137 sampling is 60 seconds for a sequence of 12 profiles and a new sequence starts 4 minutes after

138 the end of the previous one. The temporal resolution on the instrument allows for detection and

139 analysis of atmospheric processes such as the diurnal evolution of the PBL (Ricaud et al., 2012)

140 and the presence of clouds and diamond dust (Ricaud et al., 2017) together with SLWCs

141 (Ricaud et al., 2020). In addition, the LWP (g m^{-2}) that gives the amount of liquid water

142 integrated along the vertical can also be estimated. Observations of LWP have been performed

143 when the instrument was installed at the Pic du Midi station (2877 amsl, France) during the

144 calibration/validation period in 2008 prior to its set up in Antarctica in 2009 (Ricaud et al.,

145   2010a) and during the Year Of Polar Prediction (YOPP) campaign in summer 2018-2019

146   (Ricaud et al., 2020). At the present time, it has not yet been possible to compare HAMSTRAD

147   LWP retrievals with observations from other instruments, neither at the Pic du Midi nor at

148   Dome C stations. To better evaluate its performance, the 2021-2022 and the future 2022-2023

149   summer campaigns are dedicated to in-situ observations of SLWCs. Comparisons with

150   numerical weather prediction models were showing consistent amounts of LWP at Dome C

151   when the partition function between ice and liquid water was favouring SLW for temperatures

152   less than 0°C (Ricaud et al., 2020). Note that microwave observations at 60 and 183 GHz are

153   not sensitive to ice crystals. This has already been discussed in Ricaud et al. (2017) when

154   considering the study of diamond dust in Antarctica. As a consequence, possible precipitation

155   of ice, within or below SLW clouds, as detected by the Lidar, does not affect the retrievals of

156   temperature, water vapour and liquid water.

157   *2.3. BSRN*

158   The BSRN sensors at Dome C are mounted at the Astroconcordia/Albedo-Rack sites, with

159   upward and downward looking, heated and ventilated Kipp&Zonen CM22 pyranometers and

160   CG4 pyrgeometers providing measurements of hemispheric downward and upward broadband

161   shortwave (SW, 0.3–3 μm) and longwave (LW, 4–50 μm) radiative fluxes at the surface,

162   respectively. These data are used to retrieve values of net surface radiation. All these

163   measurements follow the rules of acquisition, quality check and quality control of the BSRN

164   (Driemel et al., 2018).

165   *2.4. Period of study*

166   From the climatological study presented in Ricaud et al. (2020), the SLWCs are mainly

167   observed above Dome C in summer, with a higher occurrence in December than in January:

168   26% in December against 19% in January representing the percentage of days per month that

169   SLW clouds were detected during the YOPP campaign (summer 2018-2019) within the LIDAR

170   data for more than 12 hours per day. We have thus concentrated our analysis on December and

171   the 4 years: 2018-2021. Since we have to use the three data sets (LIDAR, HAMSTRAD and

172   BSRN) in time coincidence, the actual number of days per year selected in our analysis is

173   presented in Table 1.

174

175   **3. Methodology**

176   *3.1. SLWC detection and Surface Radiation Impact*

177   Consistent with Ricaud et al. (2020), we use LIDAR observations to discriminate between

178   SLW and ice in a cloud. High values of LIDAR backscatter coefficient ($\beta > 100\ \beta_{mol}$, with β_{mol}

179   the molecular backscatter) associated with very low depolarization ratio ($< 5\%$) signifies the

180   presence of an SLWC whilst high depolarization ratio ($>20\%$) indicates the presence of an ice

181   cloud or precipitation. Once the SLWC is detected both in time and altitude, the regular

182   temperature (θ) profile within the cloud and the LWP measured by the HAMSTRAD

183   radiometer in time coincidence are selected together with the SR observed by the BSRN

184   instruments: Net, LWD, LWU, SWD and SWU SR.

185   The Lidar profiles are interpolated along the temperature vertical grid and then according

186   to the temperature time sampling. As a consequence, for a given time and height, we have a

187   depolarization ratio, a backscatter signal, a regular temperature and a (not height-dependent)

188   LWP. The same method is used for SR. BSRN SRs are time interpolated to be coincident with

189   the LWP values. So, for a given time, we have a set of BSRN SRs (Net, LWU, LWD, SWU

190   and SWD) and an LWP. At a (time, height) point showing high backscatter signal and low

191   depolarization, the associated parameters (regular temperature, LWP and SRs) are flagged as

192   "SLW cloud". The statistic is thus done using all the SLW-flagged points without any

193   averaging. The temperature corresponds to the in-cloud temperature.

194   Figure 1 shows, as a typical example, the time evolution of the LIDAR backscatter

195   coefficient and depolarization ratio, as well as the HAMSTRAD LWP and temperature vertical

196   profile for the 27 December 2021. Associated with the SLWCs, the LWP increases with time

197   from 1.0 to 3.0 g m^{-2}. The SLWCs are present over a temperature range varying from

198   about -28.0 °C to -33.0 °C. Note the cloud present at 04:00-05:00 UTC that is not labelled as a

199   SLWC but rather as an ice cloud (high backscatter and high depolarization signals) with no

200   associated increase of LWP and temperature above -28.0 °C.

201   Figure 2 highlights the time evolution of the SLWC obtained on 27 December 2021

202   together with some snapshots from the HALO-CAM video camera taken with or without SLWC

203   on: 01:00 (no SLWC), 07:19 (SLWC), 09:00 (no SLWC), 10:14 (SLWC), 13:00 (no SLWC),

204   16:03 (SLWC), 18:01 (no SLWC) and 20:53 UTC (SLWC). SLWCs (high backscatter and low

205   depolarization signals) are clearly detected at 07:00-08:00, 10:00-11:00, 16:00-17:00, 21:00-

206   22:00 and 23:00-24:00 UTC over an altitude range 500-1000 m above ground level (agl). In

207   general, SLWCs observed over the station did not correspond to overcast conditions.

208   Over the 4 summers (December 2018-2021), we have selected 3 datasets in time

209   coincidence with SLWC: LWP, θ and SR. In order to estimate the impact of the SLWC onto

210   the SR, we calculated the anomaly of the daily SR with respect to the clear-sky SR associated

211   to the same day. Since it is impossible to measure for the same day the SR with and without

212   cloud, we have in priority looked for clear-sky days over the months of December in the 2018-

213   2021 period. Only 5 clear-sky days were selected on: 2 and 19 December 2018, and 3, 17 and

214   26 December 2021. These 5 days, considered as the reference SRs (SR_{Ref}), are presented in

215   Figure 3. We have also calculated (Figure 4) the time evolution of the clear-sky surface

216   radiation variability (δSR_{Ref}), namely the difference in SR observed by the BSRN instruments

217   between each of 5 clear-sky day and the corresponding values averaged over the 5 days, for

218   Net, LWD, LWU, SWD and SWU SR. The SR_{Ref} for the 5 days shown Figure 3 are all

219 consistent to each other with an obvious diurnal cycle in Net, LWD, LWU, SWD and SWU SR

220 (we recall that in December there is a 24-h solar illumination at Dome C). The variability within

221 the 5 days (δSR_{Ref}) shown Figure 4 is within ±20 W m^{-2} for the Net SR with a greater Net SR

222 in 2018 than in 2021, within ±35 W m^{-2} for LWD and LWU SR (maxima on 17 December 2021

223 and minima on 2 December 2018), and within ±25 W m^{-2} for SWD and SWU SR (maxima on

224 26 December 2021 and minima on 2 December 2018).

225   Based on these 5 SR_{Ref}, we performed a systematic study over the 4-summer period by

226 calculating the surface radiation anomaly ΔSR defined as:

227 $$\Delta SR = SR - SR_{Ref} \qquad (2)$$

228 for Net, LWD, LWU, SWD and SWU. As an example, we show in Figure 5 the time evolution

229 for 27 December 2021 of the presence of the SLWC together with ΔSR calculated with respect

230 to SR_{Ref} set to 26 December 2021. Associated with the SLWC, LWD and LWU ΔSR increase

231 by 30-50 and 10-30 W m^{-2}, respectively, whilst SWD and SWU ΔSR decrease by 50-150 W m^{-2},

232 respectively. The effect on the Net ΔSR is positive (10-100 W m^{-2}) at 07:00-08:00, 10:00-11:00,

233 16:00-17:00 UTC and negative (from -30 to -100 W m^{-2}) at 21:00-22:00 and 23:00-24:00 UTC.

234 Note that spikes appear in Net ΔSR, SWU ΔSR and SWD ΔSR mainly during scattered

235 conditions and when large cloud episodes appear or disappear. They are real and can possibly

236 come from the inhomogeneity of the cloud distribution. We thus want to statistically analyse

237 all the ΔSR calculated in 2018-2021 with the 5 SR_{Ref} in order to check whether the net effect

238 of the SLWC on the SR is positive or negative and to evaluate its sensitivity to liquid water

239 amounts.

240 *3.2. Statistical Method*

241   The datasets are binned into 1°C-wide bins for θ, 0.2 g m^{-2}-wide bins for LWP, and

242 5 W m^{-2}-wide bins for ΔSR. The number of points per bin is calculated for all the paired

243 datasets, namely θ-LWP, and ΔSR-LWP (Net ΔSR-LWP, LWD ΔSR-LWP, LWU ΔSR-LWP,

244 SWD ΔSR-LWP and SWU ΔSR-LWP). The 2D probability density (PD) is calculated for the

245 paired datasets and defined as $PD_{ij} = 100 \frac{N_{ij}}{N_t}$, where N_{ij} and N_t are the count number in the

246 bin ij and the total count number $(N_t = \sum_{j=1}^{N} \sum_{i=1}^{M} N_{ij})$, respectively, with M and N being the

247 total number of bins in LWP on one side, and in temperature or ΔSR on the other side,

248 respectively. This study is focused on the evaluation of the LWP sensitivity for a given

249 temperature and for a given radiation component (Net, LWD, LWU, SWD, SWU). So, for each

250 value of θ_j (within a 1°C-wide bin j) or ΔSR_j (within a 5 W m^{-2}-wide bin j), a weighted average

251 of LWP $(\overline{LWP_j})$ is calculated together with its associated weighted standard deviation (σ_{LWP_j}),

252 considering all the LWP_{ij} values (within 0.2 g m^{-2}-wide bins) from i=1 to M, with M the total

253 number of LWP bins and w_{ij} the weight, namely the number of points $(w_{ij} = N_{ij})$, associated

254 to the bin ij:

$$\overline{LWP_j} = \frac{\sum_{i=1}^{M} w_{ij} \, LWP_{ij}}{\sum_{i=1}^{M} w_{ij}} \tag{3}$$

256 and

$$\sigma_{LWP_j} = \sqrt{\frac{\sum_{i=1}^{M} w_{ij} \, (LWP_{ij} - \overline{LWP_j})^2}{\sum_{i=1}^{M} w_{ij}}} \tag{4}$$

258 For each θ and ΔSR dataset, the distribution of the total count numbers N_{tj} per 1°C or

259 5 W m^{-2}-wide bin $(N_{tj} = \sum_{i=1}^{M} N_{ij}$ with $j = 1, ..., N)$ can be fitted by a function $N(x)$, with $x =$

260 θ or ΔSR, based on 2 to 3 Gaussian distributions as:

$$N(x) = \sum_{k=1}^{2 \text{ or } 3} a_k \exp\left(-\frac{1}{2}\left(\frac{x - \mu_k}{\sigma_k}\right)^2\right) + c \tag{5}$$

262 with a_k, μ_k and σ_k being the amplitude, the mean and the standard deviation of the kth Gaussian

263 function ($k = 1$, 2 or 3) and c is a constant. We have used $k = 2$ for ΔSR and $k = 3$ for θ. Table

264 2 lists all the fitted parameters (a_k, μ_k, σ_k and c with $k = 1$ to 2 or 3).

265   In the relationship between x (θ or ΔSR) and LWP, we have considered x_j (θ_j or ΔSR_j) to

266   be significant when:

267    $$|x_j - \mu_k| \leq \sigma_k \text{ for } k = 1-2 \text{ (for } \Delta SR) \text{ or } 1-3 \text{ (for } \theta) \tag{6}$$

268   and used for this significant point its average value and standard deviation, $\overline{LWP_j}$ and σ_{LWP_j},

269   respectively, with $j = 1, \ldots, N$.

270   Finally, a logarithmic function of the form

271    $$x = a + b\ln(\overline{LWP}) \tag{7}$$

272   has been fitted onto these significant points where the retrieved constants a and b are shown in

273   Table 3 for x being θ, Net ΔSR, LWD ΔSR, LWU ΔSR, SWD ΔSR and SWU ΔSR.

274

275   **4. Results**

276   *4.1. Temperature-Liquid Water Relationship in Supercooled Liquid Water Clouds*

277   The relationship between temperature and LWP within SLWCs over the 4-summer period

278   at Dome C is presented Figure 6 left in the form of a Probability Density that is the fraction of

279   points within each bin of 0.2 g m^{-2} width in LWP and 1.0°C width in temperature. It clearly

280   shows a net tendency for liquid water to increase with temperature, up to ~14 g m^{-2} in LWP and

281   -18°C in temperature, with two zones having a density as high as ~2%, at [0.5 g m^{-2}, -33°C]

282   and [1.5 g m^{-2}, -32°C]. We have performed a weighted average of the LWPs within each

283   temperature bin (Figure 6 centre). Then, we have fitted 3 Gaussian distributions to the count

284   numbers as a function of temperature (Figure 6 right). If we now only consider temperature

285   bins within one-sigma of the centre of the Gaussian distributions, we can fit the following

286   logarithmic relation of the temperature θ as a function of LWP within the SLWC (Figure 6

287   centre):

288    $$\theta(LWP) = -33.8\ (\pm1.5) + 6.5\ln(LWP) \tag{8}$$

289 for $\theta \in [-36; -16]$ °C and $LWP \in [1.0; 14.0]$ g m⁻², where (± 1.5 °C) corresponds to the

290 range where the relationship is valid within the 2 blue dashed lines in Figure 6 centre. In other

291 words, based on our study, we have a clear evidence that supercooled liquid water content

292 exponentially increases with temperature. Considering the temperature vs. LWP relationship,

293 the 2 main Gaussian distributions are centred around -28°C and -30°C, corresponding to

294 temperatures usually encountered in Concordia whilst the third one, far much less intense, is

295 centred around -18°C, probably the signature of very unusual events occurring in Concordia as

296 the warm-moist events. Episodes of warm-moist intrusions exist above Concordia originated

297 from mid-latitudes (Ricaud et al., 2017 and 2020) and are known as "atmospheric rivers" (Wille

298 et al., 2019). Although they are infrequent, they can provide high values of temperature and

299 LWP.

300 *4.2. Impacts of Supercooled Liquid Water Clouds on Surface Radiation*

301 Although the amount of LWP is very low ($\ll 20$ g m⁻²) at Dome C compared to what can

302 be measured and modelled (Lemus et al., 1997) in the Arctic (50-75 g m⁻²) and at

303 middle/tropical latitudes (100-150 g m⁻²), we intended to estimate its impact on the SR at Dome

304 C. In Figures 7 to 9, the left panel presents the PDs (for bins of 0.2 g m⁻² width in LWP and 5

305 W m⁻² width in ΔSR) of the surface radiation anomaly ΔSR as a function of the LWP, for Net,

306 LWD, LWU, SWD and SWU, respectively. The central panel shows, for the same parameters,

307 the corresponding weighted average LWP within 5 W m⁻²-wide bins of radiation anomaly

308 whereas the right panel shows the corresponding count number within 5 W m⁻²-wide bins fitted

309 by 2 Gaussian distributions.

310 Based on our analysis, the relationship between Net ΔSR (in W m⁻²) and the LWP (in g m⁻²)

311 has been estimated from the HAMSTRAD and BSRN data as:

312 $$Net\ \Delta SR(LWP) = -50.0\ (\pm 10.0)\ + 90.0\ln(LWP) \qquad (9)$$

313 for $Net\ \Delta SR \in [-15; 50]$ W m^{-2} and $LWP \in [1.5; 3.0]$ g m^{-2}, where (± 10.0 W m^{-2})

314 corresponds to the range where the relationship is valid within the 2 blue dashed lines in Figure

315 7 centre. Thus, for LWP greater than 1.7 g m^{-2}, our study clearly shows that there is a positive

316 impact of SLWC on the Net ΔSR that can reach 50 W m^{-2} for an LWP of 3.0 g m^{-2}.

317 The splitting of the net radiation anomaly between each of its four components can be

318 evaluated from their individual relationships with the LWP. These relations are gathered in

319 Table 3, established from the plots presented in Figures 7 to 9. They are of the same form as

320 for net surface radiation anomaly, i.e. a logarithmic dependence on LWP. Table 3 presents the

321 coefficients a and b of the logarithmic function $f(LWP) = a + b\ln(LWP)$ for the temperature

322 θ or the radiation components ΔSR, together with the valid range of these relations for $\theta, \Delta SR$

323 and LWP. For the values presented in Table 3, our study clearly shows that SLWCs have a

324 positive impact on LWD and LWU, with ΔSR increasing from 0 to 100 W m^{-2} and from 0 to

325 40 W m^{-2} for LWP ranging from 1.0 to 4.0 and from 1.6 to 2.5 g m^{-2}, respectively. Considering

326 the SR vs. LWP relationship, it seems that we have systematically one of the Gaussian

327 distributions centred around 0 W m^{-2}, reflecting the non-impacting part of SLWCs on SR

328 components.

329 Furthermore, our study also shows that SLWCs have a clear negative impact on SWD and

330 SWU, with ΔSR decreasing from 0 to -140 W m^{-2} and from 0 to -75 W m^{-2} with LWP ranging

331 from 1.2 to 3.8 and from 1.2 to 3.2 g m^{-2}, respectively.

332

333 **5. Discussion**

334 *5.1 Relation with critical temperature*

335 Note that the relationships show an exponential dependence of LWP on both temperature

336 and SR anomaly similar to the dependence of the molar volume and density of water on critical

337   temperature. As a matter of fact, the density ρ (g cm^{-3}) and molar volume ν (cm^3 mol^{-1}) of liquid

338   water are exponentially varying with temperature (Sippola and Taskinen, 2018):

339
$$\rho = \rho_0 \exp\{-T_c(A + B\varepsilon + 2C\varepsilon^{1/2})\} \qquad (13)$$

340
$$\nu = \frac{M_{H_2O}}{\rho} = \frac{M_{H_2O}}{\rho_0}\exp\{T_c(A + B\varepsilon + 2C\varepsilon^{1/2})\} \qquad (14)$$

341   where ρ_0 (g cm^{-3}), A (K^{-1}), B (K^{-1}), and C (K^{-1}) are parameters; T_c is the critical temperature

342   whose value varies from 227 to 228 K, and M_{H_2O} (g mol^{-1}) is the molecular weight of water.

343   ε (unitless) is defined as:

344
$$\varepsilon = \frac{T}{T_c} - 1 \qquad (15)$$

345   where T is temperature in K.

346

347   *5.2. Reference Surface Radiation and sastrugi effect*

348   In order to evaluate the surface radiation in clear-sky conditions at Concordia, we have

349   used, in complement to BSRN observations, and at the closest location to Concordia station,

350   two different data sets of surface radiations from i) the European Center for Medium-Range

351   Weather Forecasts Reanalysis version 5 (ERA5). ERA5 is a climate reanalysis dataset, covering

352   the period 1979 to present. ERA5 is being developed through the Copernicus Climate Change

353   Service (C3S). Extracted data (https://cds.climate.copernicus.eu/cdsapp#!/dataset/reanalysis-

354   era5-single-levels) used here are hourly at a regular horizontal grid of 0.25°x0.25° in clear-sky

355   conditions: surface solar and thermal infrared, downward and net radiations. As explained on

356   the ERA5 website, clear-sky radiations are computed for the same atmospheric conditions of

357   temperature, humidity, ozone, trace gases and aerosol as the corresponding total-sky quantities

358   (clouds included), but assuming that the clouds are not there; ii) the Clouds and the Earth's

359   Radiant Energy System (CERES), containing SYN1deg (Hourly CERES and geostationary

360   (GEO) TOA fluxes, MODIS/VIIRS and GEO cloud properties, MODIS/VIIRS aerosols, and

361 Fu-Liou radiative transfer surface and in-atmospheric (profile) fluxes consistent with the

362 CERES observed TOA fluxes, as explained on https://ceres.larc.nasa.gov/data/). Surface fluxes

363 in SYN1deg are computed with cloud properties derived from MODIS and geostationary

364 satellites (GEO), where each geostationary satellite instrument is calibrated against MODIS

365 (Doelling et al. 2013; 2016) at 1°x1° horizontal resolution (https://ceres.larc.nasa.gov/data/).

366 Aerosol and atmospheric data were included as inputs to calculate the radiation flux.

367 We have compared the CERES and ERA5 data with the BSRN hourly-averaged data on

368 the 5 reference days (clear-sky conditions) for the Net, LWD, LWU, SWD and SWU SRs.

369 Figure 10 shows these variables for the 26 December 2021. The LWD and LWU values show

370 an overall consistency between ERA5 and CERES (of the order of ~10 W m-2), while a

371 systematic negative bias of ~20-40 W m-2 is observed with respect to BSRN data. However,

372 the net longwave radiation, i.e. the difference LWD – LWU for each data set, is reduced to

373 around 5 W m^{-2}. The SWD and SWU signals from ERA5, CERES and BSRN show a similar

374 diurnal variation with differences less than 50 W m^{-2}. When considering the Net SR, some

375 obvious differences up to 50 W m^{-2} can be seen between BSRN, ERA5 and CERES. Since the

376 net longwave radiation is within 10 W m^{-2} for the three data sets, the source of this difference

377 therefore should come from either SWD or SWU radiation. We have calculated, for BSRN,

378 ERA5 and CERES data, the albedo defined as:

379 $$albedo = \frac{SWU}{SWD} \qquad (10)$$

380 Figure 11 shows the diurnal evolution of the albedo on 26 December 2021 (clear-sky day).

381 The CERES and ERA5 albedos do not show any significant diurnal variation with quite

382 constant values of 0.74 and 0.83, respectively, whilst the observed BSRN albedo shows a clear

383 diurnal signal with a maximum of 0.85 from 10:00 to 14:00 UTC (from 18:00 to 22:00 LT) and

384 a minimum of 0.70 from 19:00 to 23:00 UTC (from 03:00 to 07:00 LT). The large diurnal signal

385 present in the observed albedo is likely the signature of the sastrugi effect that is obviously

absent in the ERA5 and CERES data sets. The BSRN SWU sensor has a circular footprint. For a sensor installed at a height h above the ground, 90% of the signal comes from an area at the surface closer than 3.1 h (Kassianov et al., 2014). Since at Dome-C the instrument is installed at a height of 2-3 m, the albedo is thus determined by the surface elements in the immediate vicinity (a few meters) of the sensor.

Sastrugi (Figure 12) are features formed by erosion of snow by wind. They are found in polar regions, and in snowy, wind-swept areas of temperate regions, such as frozen lakes or mountain ridges. Sastrugi are distinguished by upwind-facing points, resembling anvils, which move downwind as the surface erodes.

We have fitted the BSRN albedo averaged over the 5 reference days with the sum of 2 sine functions, imposing periods of 24 and 12 hours. Figure 13 shows the BSRN albedo averaged over the five clear-sky days, the fitted trigonometric function and the residuals between the averaged albedo and the fitted function. We can state that the sastrugi effect on the observed clear-sky albedo at Concordia is successfully fitted by 2 sine functions of 24h and 12h periods to within 0.003 mean absolute error, with a coefficient of determination R^2 equal to 0.993 and a root mean square error of 0.0004.

If we suppose that the sastrugi effect impacts mostly SWU rather than SWD, and the albedo calculated from BSRN observations is the "truth", we can calculate a modified SWU* (including the sastrugi effect) for the ERA5 and CERES as:

$$SWU(ERA5)^* = SWD(ERA5) \times albedo(BSRN) \tag{11}$$

$$SWU(CERES)^* = SWD(CERES) \times albedo(BSRN) \tag{12}$$

Then we calculate the modified Net SR* (including the sastrugi effect) considering SWU* for ERA5 and CERES. As an example, we present Figure 14, similar to Figure 10, in which we added the albedo and the SWU* and Net SRs* (including the sastrugi effect) for CERES and ERA5 (solid lines). We observe that the Net SR* for ERA5 and CERES now coincides with

411 the BSRN Net SR to within 5 W m^{-2}, compared to differences up to 50 W m^{-2} found when the

412 sastrugi effect was not taken into account.

413 Moreover, we have considered all the BSRN observations in Decembers 2018, 2019, 2020

414 and 2021 to calculate the albedo (Figure 15), and we have superimposed the fitted trigonometric

415 function as described in Figure 13. The presence of clouds is well highlighted by observations

416 that depart from the fitted function whilst, during periods of clear-sky conditions, BSRN

417 albedos coincide well with the fitted function.

418 The study we have performed was extremely fruitful to evaluate the impact of the SLW

419 clouds on the SR. The methodology requires reference clear-sky SR values that can be

420 evaluated from: 1) models, 2) analyses and 3) observations. Our study has mainly shown that,

421 at the Concordia station, sastrugi were present and strongly impacted the net SR via the surface

422 albedo. This very local phenomenon cannot be taken into account by either the global-scale

423 analyses (ERA5 and CERES), or standard radiative transfer models (e.g. RRTMG). As a

424 consequence, the methodology we have developed based on field observations is likely the most

425 powerful tool to estimate the Net SR in Concordia. It has some drawbacks, as for instance some

426 biases for LWD and LWU between analyses and observations, but the LWD and LWU

427 difference used to calculate the Net SR dramatically lessens the bias.

428 *5.3. Modelling SLWC*

429 Previous studies have already underlined the difficulty to model the SLWC together with

430 its impact on surface radiations. Modelling SLWCs over Antarctica is challenging because 1)

431 operational observations are scarce since the majority of meteorological radiosondes are

432 released from ground stations located at the coast and very few of them are maintained all year

433 long, and satellite observations are limited to 60°S in geostationary orbit whilst, in polar orbit,

434 the number of available orbits does not exceed 15 per day, and 2) the model should provide a

435 partition function favouring liquid water at the expense of ice for temperatures between -36°C

436   and 0°C in order to calculate realistic SLW contents. Differences of 20 to 50 W m^{-2} in the Net

437   SR were found in the Arpege model (Pailleux et al., 2015) between clouds made of ice or liquid

438   water during the summer 2018-2019 (Ricaud et al., 2020), differences that are very consistent

439   with the results obtained in the present study. Although SLWCs are less present over the

440   Antarctic Plateau than over the coastal region, their radiative impact is not negligible and should

441   be taken into account with great care in order to estimate the radiative budget of the Antarctic

442   continent in one hand, and, on the other hand, over the entire Earth.

443   *5.4. Errors*

444   Measurements of temperature, LWP, depolarization signal and SR are altered by random

445   and systematic errors that may affect the relationships we have obtained between LWP and

446   either temperature or SR anomalies. The temperature measured by HAMSTRAD below 1 km

447   has been evaluated against radiosonde coincident observations from 2009 to 2014 (Ricaud et

448   al., 2015) and the resulting bias is 0-2°C below 100 m and between -2 and 0°C between 100

449   and 1000 m. SLWCs are usually located around 400-600 m above the ground where the cold

450   bias can be estimated to be about -1.0°C. The one-sigma (1-σ) RMS temperature error over a

451   7-min integration time is 0.25°C in the PBL and 0.5°C in the free troposphere (Ricaud et al.,

452   2015). As a consequence, given the number of points used in the statistical analysis (>1000),

453   the random error on the weighted-average temperature is negligible (<0.02°C). The LWP

454   random and systematic errors are difficult to evaluate since there is no coincident external data

455   to compare with. Nevertheless, the 1-σ RMS error over a 7-min integration time can be

456   estimated to be 0.25 g m^{-2} giving a random error on the weighted average LWP less than 0.08

457   g m^{-2}. Based on clear-sky observations, the positive bias can be estimated to be less than

458   0.4 g m^{-2}. Theoretically, SLW should not exist at temperatures less than -39°C although it has

459   been observed in recent laboratory measurements down to -42.55°C (Goy et al., 2018). Using

460   equation (8) with an LWP bias of 0.4 g m^{-2} gives a temperature of -39.8°C (~0.8°C lower than

461   the theoretical limit of -39°C), so the biases estimated for temperature and LWP are very

462   consistent with theory.

463   The estimation of systematic and random errors on LIDAR backscattering and

464   depolarization signals and their impact on the attribution/selection of SLWC is not trivial. But

465   the most important point is to evaluate whether the observed cloud is constituted of purely liquid

466   or mixed-phase water. Even considering the backscatter intensity only, we could not exclude

467   that ice particles could have been present in the SLWC events investigated in 2018 (Ricaud et

468   al., 2020). Therefore, in the present analysis, although we made a great attention to diagnose

469   ice in the LIDAR cloud observations, we cannot totally exclude ice particles thus mixed-phase

470   parcels were actually present when we labelled the observed cloud as SLWCs.

471   The 4 instruments providing LWD, LWU, SWD and SWU SR follow the rules of

472   acquisition, quality check and quality control of the BSRN (Driemel et al., 2018). These data

473   are often considered as a reference against which products based on satellite observations and

474   radiative transfer models (such as e.g. CERES) are validated (Kratz et al., 2020). In polar

475   regions (Lanconelli et al., 2011), SWU and SWD SRs are expected to be affected by random

476   errors up to ± 20 W m^{-2} while LWD SRs are expected to be affected by random errors not greater

477   than ± 10 W m^{-2} (Ohmura et al., 1998). As a consequence, given the large number of

478   observations used per 5 W m^{-2}-wide bins (1000-3000), the random error on the weighted-

479   average SRs is negligible (0.3-0.7 W m^{-2}) whatever the radiations considered, LW and SW.

480   Finally, apart from the instrument-related SR_{Ref} error, another source of error comes from

481   1) the geometry of observation and 2) the discontinuous SLWC layer. Firstly, LIDAR is almost

482   zenith pointing, HAMSTRAD makes a scan in the East direction (from 10° elevation to zenith),

483   whilst the BSRN radiometers detect the radiation in a 2π-steradians field of view (3D

484   configuration). That is to say, in our analysis, the whole sky contributes to the radiation whilst

485   only the cloud at zenith (1D configuration) and on the East direction (2D configuration) is

486 observed by the LIDAR and HAMSTRAD, respectively. Secondly, SLWCs cannot be

487 considered as uniform in the whole (see e.g. broken cloud fields in Figure 2).

488 *5.5. Other clouds*

489   Although the method we have developed to select the SLWCs has been validated using the

490 amount of LWP and, in another study, using space-borne observations (Ricaud et al., 2020), we

491 cannot rule out that, associated with the SLW droplets, are also ice particles, that is clouds are

492 constituted of a mixture of liquid and solid water. Generally, such clouds are a superposition of

493 a lower layer being made of liquid water and an upper layer being made of solid water (see Fig.

494 12.3 from Lamb and Verlinde, 2011). These mixed-layer clouds do not significantly modify the

495 relationship between temperature and LWP because 1) SLW observations from HAMSTRAD

496 are only sensitive to water in liquid phase and 2) temperature from HAMSTRAD is selected at

497 times and vertical heights where the LIDAR depolarization signal is very low (<5%). Although

498 we have verified that pure ice clouds were not selected by our method, we cannot differentiate

499 mixed-phase clouds from purely SLWCs. As a consequence, the presence of mixed-phase

500 clouds in addition to SLWCs may explain the negative part of the Net, LWD and LWU ΔSR

501 ([-20;0] W m^{-2}) and the positive part of the SWD and SWU ΔSR ([0;10] W m^{-2}) for low

502 values of LWP ([0.8;1.6] g m^{-2}).

503   Furthermore, we already have noticed that SLWCs developed at the top of the PBL (Ricaud

504 et al., 2020) in the "entrainment zone" and maintained in the "capping inversion zone",

505 following the terminology of Stull (1988), at a height ranging from 100 to 1000 m above ground

506 level. Nevertheless, during the local "night" at 00:00-06:00 LT, the PBL may collapse down to

507 a very low height ranging 20-50 m. In this configuration, it is hard to differentiate from LIDAR

508 observations between a SLWC and a fog episode, although the LIDAR can measure

509 depolarization (but not backscatter) down to approximately 10-30 m above the ground (Figure

510 S3 in Chen et al., 2017), so that we can distinguish liquid/frozen clouds very close to the ground.

511   Finally, we cannot rule out that, above the SLWCs that are actually observed by both

512   LIDAR and HAMSTRAD, other clouds might be present, as e.g. cirrus clouds constituted of

513   ice crystals. These mid-to-upper tropospheric clouds cannot be detected by HAMSTRAD (no

514   sensitivity to ice crystals). In the presence of SLWCs either low in altitude or optically thick,

515   the LIDAR backscatter signal is decreased in order to avoid saturation and the signal from upper

516   layers is thus almost cancelled. These mid-to-high-altitude clouds are observed by the BSRN

517   instruments and SR can be affected in this configuration. Based on the presence of cirrus clouds

518   before or after the SLWCs (and sometimes during the SLWCs if optically thin), we can estimate

519   that the number of days when SLWCs and cirrus clouds are simultaneously present to cover

520   less than 10% of our period of interest.

521   *5.6. Potential radiative impact of SLWCs over Antarctica*

522   Based on 2007-2010 reanalyses, observations and climate models (Lenaerts et al., 2017),

523   LWP over Antarctica is on average less than 10 g m^{-2}, with slightly larger values in summer

524   than in winter by 2-5 g m^{-2}. Over Western Antarctica, LWPs are larger (20-40 g m^{-2}) than over

525   Eastern Antarctica (0-10 g m^{-2}). As a consequence, LWPs observed at Concordia are consistent

526   with values observed over the Eastern Plateau, with a factor 2-4 smaller than those observed

527   over the Western continent. Based on our results and on the observed cloud fraction (η_{CF}) of

528   SLWCs over Antarctica for different seasons (Listowski et al., 2019), we have estimated the

529   potential radiative impact of SLWCs at the scale of the Antarctic continent ($Net\ \Delta SR_{global}^{max}$)

530   from the maximum of $Net\ \Delta SR$ ($Net\ \Delta SR^{max} = 50$ W m^{-2}) computed in our study:

531   $$Net\ \Delta SR_{global}^{max} = \eta_{CF} \times\ Net\ \Delta SR^{max} \qquad (13)$$

532   In summer, η_{CF} is varying from 5% in Eastern Antarctica to 40% in Western Antarctica whilst,

533   in winter, it is varying from 0% in Eastern Antarctica to 20% in Western Antarctica (Listowski

534   et al., 2019). In December, if we consider η_{CF} for SLW-containing cloud (that is to say both

535   mixed-phase cloud and unglaciated SLW cloud consistent with our study), we find for a lower-

536   level altitude cut-off of 0, 500 and 1000 m (Figure B1 in Listowski et al., 2019), a potential

537   radiative impact $Net\ \Delta SR_{global}^{max}$ over Antarctica of 9, 7 and 5 W m^{-2}, respectively. We now

538   separate the Eastern elevated Antarctic Plateau from the Western Antarctica (Figure 5 in

539   Listowski et al., 2019) for the 4 seasons. Over Eastern Antarctica, we find that $Net\ \Delta SR_{global}^{max} =$

540   0.5-5.0 W m^{-2} in December-January-February (DJF) and 0-2.5 W m^{-2} for the remaining

541   seasons. Over Western Antarctica, the potential radiative impact is much more intense because

542   of higher temperatures and lower elevations compared to the Eastern Antarctic Plateau:

543    $Net\ \Delta SR_{global}^{max} =$ 12.5-30.0 W m^{-2} in DJF (30 W m^{-2} over the Antarctica Peninsula); 7.5-20.0

544   W m^{-2} in March-April-May; 2.5-10.0 W m^{-2} in June-July-August; and 5.0-12.5 W m^{-2} in

545   September-October-November.

546

547   **6. Conclusions**

548   Combining the observations of temperature, water vapour and liquid water path from a

549   ground-based microwave radiometer, backscattering and depolarization from a ground-based

550   LIDAR and surface radiations at long and short wavelengths, our analysis has been able to

551   evaluate the presence of supercooled liquid water clouds over the Dome C station in summer.

552   Focusing on the month of December in 2018-2021, we established that in SLWCs temperature

553   logarithmically increases from -36.0°C to -16.0°C when LWP increases from 1.0 to 14.0 g m^{-2}.

554   We have also evaluated that SLWCs positively affect the net SR, which logarithmically

555   increases from 0.0 to 50.0 W m^{-2} when LWP increases from 1.7 to 3.0 g m^{-2}. Our study clearly

556   shows that: 1) SLWCs have a positive impact on LWD and LWU, with ΔSR increasing from 0

557   to 100 W m^{-2} and from 0 to 40 W m^{-2} for LWP ranging from 1.0 to 4.0 and from 1.6 to 2.5 g m^{-2},

558   respectively, and 2) SLWCs have a clear negative impact on SWD and SWU, with ΔSR

559   decreasing from 0 to -140 W m^{-2} and from 0 to -75 W m^{-2} with LWP ranging from 1.2 to 3.8

560   and from 1.2 to 3.2 g m^{-2}, respectively.

561   Our study has ~~mainly~~ shown that, at the Concordia station, sastrugi were present and

562   strongly impacted the net SR via the surface albedo. This very local phenomenon cannot be

563   taken into account by either the global-scale analyses (ERA5 and CERES), or standard radiative

564   transfer models. As a consequence, the methodology we have developed based on field

565   observations is likely the most powerful tool to estimate the Net SR in Concordia. It has some

566   drawbacks, as for instance some biases for LWD and LWU between analyses and observations,

567   but the LWD – LWU difference that is used to calculate the Net SR dramatically lessens the

568   bias.

569   Finally, extrapolating the radiative impact of the SLWCs from the Dome C station to the

570   Antarctic continent shows that SLWCs have a great potential radiative impact all over

571   Antarctica whatever the season considered, up to 5.0 W m^{-2} over the Eastern Antarctic Plateau

572   and up to 30 W m^{-2} over the Antarctic Peninsula in summer season. This stresses the importance

573   of accurately modelling SLWCs when calculating the Earth energy budget to adequately

574   forecast the Earth climate evolution, especially since the climate is rapidly changing in

575   Antarctica, as illustrated by the surface temperature record of -12°C recently observed in March

576   2022   at   the   Concordia   station   and   largely   publicized   worldwide   (see   e.g.

577   https://www.9news.com.au/world/antarctica-heatwave-extreme-warm-weather-recorded-

578   concordia-research-station/3364dd91-2051-4df5-8cfc-5f2819058604).

579

580   **Data availability**

581   HAMSTRAD data are available at http://www.cnrm.meteo.fr/spip.php?article961&lang=en

582   (last access: 3 May 2022). The tropospheric depolarization LIDAR data are reachable at

583   http://lidarmax.altervista.org/lidar/home.php (last access: 3 May 2022). Radiosondes are

584   available at http://www.climantartide.it (last access: 3 May 2022). BSRN data can be obtained

585   from the ftp server (https://bsrn.awi.de/data/data-retrieval-via-ftp/) (last access: 3 May 2022).

586

Author contribution

588 PR, MDG, and AL provided the observational data. PR developed the methodology. All the
589 co-authors participated in the data analysis and in the data interpretation. PR prepared the
590 manuscript with contributions from all co-authors.

591

Competing interests

593 The authors declare that they have no conflict of interest.

594

Acknowledgments

596 The present research project Water Budget over Dome C (H2O-DC) has been approved by
597 the Year of Polar Prediction (YOPP) international committee. The HAMSTRAD programme
598 (910) was supported by the French Polar Institute, Institut polaire français Paul-Emile Victor
599 (IPEV), the Institut National des Sciences de l'Univers (INSU)/Centre National de la Recherche
600 Scientifique (CNRS), Météo-France and the Centre National d'Etudes Spatiales (CNES). The
601 permanently manned Concordia station is jointly operated by IPEV and the Italian Programma
602 Nazionale Ricerche in Antartide (PNRA). The tropospheric LIDAR operates at Dome C from
603 2008 within the framework of several Italian national (PNRA) projects. We would like to thank
604 all the winterover personnel who worked at Dome C on the different projects: HAMSTRAD,
605 aerosol LIDAR and BSRN. We would like to thank the two anonymous reviewers for their
606 beneficial comments.

607

References

609 Bergeron, T., 1928: Über die dreidimensional verknüpfende Wetteranalyse. – Geophys. Norv.

610   Bromwich, D. H., Nicolas, J. P., Hines, K. M., Kay, J. E., Key, E. L., Lazzara, Lubin, D.,

611   McFarquhar, G. M., Gorodetskaya, I. V., Grosvenor, D. P., Lachlan-Cope, T., and van

612   Lipzig, N. P. M.: Tropospheric clouds in Antarctica, Rev. Geophys., 50, RG1004,

613   https://doi.org/10.1029/2011RG000363, 2012.

614   Bromwich, D. H., Otieno, F. O., Hines, K. M., Manning, K. W., and Shilo, E.: Comprehensive

615   evaluation of polar weather research and forecasting model performance in the Antarctic, J.

616   Geophys. Res.-Atmos., 118, 274–292, 2013.

617   Chen, X., Virkkula, A., Kerminen, V.-M., Manninen, H. E., Busetto, M., Lanconelli, C., Lupi,

618   A., Vitale, V., Del Guasta, M., Grigioni, P., Väänänen, R., Duplissy, E.-M., Petäjä, T., and

619   Kulmala, M.: Features in air ions measured by an air ion spectrometer (AIS) at Dome C,

620   Atmos. Chem. Phys., 17, 13783–13800, https://doi.org/10.5194/acp-17-13783-2017, 2017.

621   Clough, S. A., M. W. Shephard, E. J. Mlawer, J.S. Delamere, M. J. Iacono, K. Cady-Pereira, S.

622   Boukabara, and P. D. Brown. Atmospheric radiative transfer modeling: A summary of the

623   aer codes. J. Quant. Spectrosc. Radiat. Transfer, 91:233–244, 2005.

624   Doelling, D. R., N. G. Loeb, D. F. Keyes, M. L. Nordeen, D. Morstad, C. Nguyen, B. A.

625   Wielicki, D. F. Young, M. Sun, 2013: Geostationary Enhanced Temporal Interpolation for

626   CERES Flux Products, Journal of Atmospheric and Oceanic Technology, 30(6), 1072-1090.

627   doi: 10.1175/JTECH-D-12-00136.1.

628   Doelling, D. R., M. Sun, L. T. Nguyen, M. L. Nordeen, C. O. Haney, D. F. Keyes, P. E.

629   Mlynczak, 2016: Advances in Geostationary-Derived Longwave Fluxes for the CERES

630   Synoptic (SYN1deg) Product, Journal of Atmospheric and Oceanic Technology, 33(3),

631   503-521. doi: 10.1175/JTECH-D-15-0147.1.

632   Driemel, A., Augustine, J., Behrens, K., Colle, S., Cox, C., Cuevas-Agulló, E., Denn, F. M.,

633   Duprat, T., Fukuda, M., Grobe, H., Haeffelin, M., Hodges, G., Hyett, N., Ijima, O., Kallis,

634   A., Knap, W., Kustov, V., Long, C. N., Longenecker, D., Lupi, A., Maturilli, M., Mimouni,

635   M., Ntsangwane, L., Ogihara, H., Olano, X., Olefs, M., Omori, M., Passamani, L., Pereira,

636   E. B., Schmithüsen, H., Schumacher, S., Sieger, R., Tamlyn, J., Vogt, R., Vuilleumier, L.,

637   Xia, X., Ohmura, A., and König-Langlo, G.: Baseline Surface Radiation Network (BSRN):

638   structure and data description (1992–2017), Earth Syst. Sci. Data, 10, 1491–1501,

639   https://doi.org/10.5194/essd-10-1491-2018, 2018.

640   Findeisen, W., 1938: Kolloid-meteorologische Vorgänge bei Niederschlagsbildung. Meteorol.

641   Z. 55, 121–133. (translated and edited by Volken, E., A.M. Giesche, S. Brönnimann. –

642   Meteorol. Z. 24 (2015), DOI:10.1127/metz/2015/0675).

643   Goy, C., Potenza, M. A., Dedera, S., Tomut, M., Guillerm, E., Kalinin, A., Voss, K.-O.,

644   Schottelius, A., Petridis, N., Prosvetov, A., Tejeda, G., Fernández, J. M., Trautmann, C.,

645   Caupin, F., Glasmacher, U., and Grisenti, R. E.: Shrinking of rapidly evaporating water

646   microdroplets reveals their extreme supercooling, Phys. Rev. Lett., 120, 015501,

647   https://doi.org/10.1103/PhysRevLett.120.015501, 2018.

648   Grazioli, J., Genthon, C., Boudevillain, B., Duran-Alarcon, C., Del Guasta, M., Madeleine, J.-

649   B., and Berne, A.: Measurements of precipitation in Dumont d'Urville, Adélie Land, East

650   Antarctica, The Cryosphere, 11, 1797–1811, https://doi.org/10.5194/tc-11-1797-2017,

651   2017.

652   Grosvenor, D. P., Choularton, T. W., Lachlan-Cope, T., Gallagher, M. W., Crosier, J., Bower,

653   K. N., Ladkin, R. S., and Dorsey, J. R.: In-situ aircraft observations of ice concentrations

654   within clouds over the Antarctic Peninsula and Larsen Ice Shelf, Atmos. Chem. Phys., 12,

655   11275–11294, https://doi.org/10.5194/acp-12-11275-2012, 2012.

656   Hogan, R. J. and Illingworth, A. J.: The effect of specular reflection on spaceborne lidar

657   measurements of ice clouds, Report of the ESA Retrieval algorithm for EarthCARE project,

658   5 pp., 2003.

Kassianov E, Barnard J, Flynn C, Riihimaki L, Michalsky J, Hodges G (2014) Areal-averaged spectral surface albedo from ground-based transmission data alone: toward an operational retrieval. Atmosphere 5:597–621. https://doi.org/10.3390/atmos503059)

King, J. C., Argentini, S. A., and Anderson, P. S.: Contrasts between the summertime surface energy balance and boundary layer structure at Dome C and Halley stations, Antarctica, J. Geophys. Res.-Atmos., 111, D02105, https://doi.org/10.1029/2005JD006130, 2006.

King, J. C., Gadian, A., Kirchgaessner, A., Kuipers Munneke, P., Lachlan-Cope, T. A., Orr, A., Reijmer, C., Broeke, M. R., van Wessem, J. M., and Weeks, M.: Validation of the summertime surface energy budget of Larsen C Ice Shelf (Antarctica) as represented in three high-resolution atmospheric models, J. Geophys. Res.-Atmos., 120, 1335–1347, https://doi.org/10.1002/2014JD022604, 2015.

Kratz, D. P., Gupta, S. K., Wilber, A. C., and Sothcott, V. E.: Validation of the CERES Edition-4A Surface-Only Flux Algorithms, J. Appl. Meteorol. Clim., 59, 281–295, https://doi.org/10.1175/JAMC-D-19-0068.1, 2020.

Lachlan-Cope, T.: Antarctic clouds, Polar Res., 29, 150–158, 2010.

Lachlan-Cope, T., Listowski, C., and O'Shea, S.: The microphysics of clouds over the Antarctic Peninsula – Part 1: Observations, Atmos. Chem. Phys., 16, 15605–15617, https://doi.org/10.5194/acp-16-15605-2016, 2016.

Lamb, D., and J. Verlinde: Physics and chemistry of clouds. Cambridge University Press, 2011.

Lanconelli, C., Busetto, M., Dutton, E. G., König-Langlo, G., Maturilli, M., Sieger, R., Vitale, V., and Yamanouchi, T.: Polar baseline surface radiation measurements during the International Polar Year 2007–2009, Earth Syst. Sci. Data, 3, 1–8, https://doi.org/10.5194/essd-3-1-2011, 2011.

Lawson, R. P. and Gettelman, A.: Impact of Antarctic mixed-phase clouds on climate, P. Natl. Acad. Sci. USA, 111, 18156–18161, 2014.

684   Legrand, M., Yang, X., Preunkert, S., and Therys, N.: Year-round records of sea salt, gaseous,

685   and particulate inorganic bromine in the atmospheric boundary layer at coastal (Dumont

686   d'Urville) and central (Concordia) East Antarctic sites, J. Geophys. Res. Atmos., 121, 997–

687   1023, https://doi.org/10.1002/2015JD024066, 2016.

688   Lemus, L., Rikus, L., Martin, C., and Platt, R.: Global cloud liquid water path simulations. J.

689   Climate, 10(1), 52-64, 1997.

690   Lenaerts, J. T., Van Tricht, K., Lhermitte, S. and L'Ecuyer, T. S.: Polar clouds and radiation in

691   satellite observations, reanalyses, and climate models, Geophysical Research Letters, 44(7),

692   3355-3364, 2017.

693   Listowski, C. and Lachlan-Cope, T.: The microphysics of clouds over the Antarctic Peninsula

694   – Part 2: modelling aspects within Polar WRF, Atmos. Chem. Phys., 17, 10195–10221,

695   https://doi.org/10.5194/acp-17-10195-2017, 2017.

696   Listowski, C., Delanoë, J., Kirchgaessner, A., Lachlan-Cope, T., and King, J.: Antarctic clouds,

697   supercooled liquid water and mixed phase, investigated with DARDAR: geographical and

698   seasonal variations, Atmos. Chem. Phys., 19, 6771–6808, https://doi.org/10.5194/acp-19-

699   6771-2019, 2019.

700   Lubin, D., Chen, B., Bromwich, D. H., Somerville, R. C., Lee, W. H., and Hines, K. M.: The

701   Impact of Antarctic Cloud Radiative Properties on a GCM Climate Simulation, J. Climate,

702   11, 447-462, 1998.

703   Mishchenko, M. I., Hovenier, J. W., and Travis, L. D. (Eds.): Light Scattering by Nonspherical

704   Particles: Theory, Measurements, and Applications, Academic Press, chap. 14, 393–416,

705   2000.

706   Ohmura, A., Dutton, E. G., Forgan, B., Fröhlich, C., Gilgen, H., Hegner, H., Heimo, A., König-

707   Langlo, G., McArthur, B., Müller, G., Philipona, R., Pinker, R., Whitlock, C. H., Dehne,

708   K., and Wild, M.: Baseline Surface Radiation Network (BSRN/WCRP): New precision

709   radiometry for climate research, B. Am. Meteorol. Soc., 79(10), 2115-2136, 1998.

710   O'Shea, S. J., Choularton, T. W., Flynn, M., Bower, K. N., Gallagher, M., Crosier, J., Williams,

711   P., Crawford, I., Flem- ing, Z. L., Listowski, C., Kirchgaessner, A., Ladkin, R. S., and

712   Lachlan-Cope, T.: In situ measurements of cloud microphysics and aerosol over coastal

713   Antarctica during the MAC campaign, Atmos. Chem. Phys., 17, 13049–13070,

714   https://doi.org/10.5194/acp-17-13049-2017, 2017.

715   Pailleux, J., Geleyn, J.-F., El Khatib, R., Fischer, C., Hamrud, M., Thépaut, J.-N., Rabier, F.,

716   Andersson, E., Salmond, D., Burridge, D., Simmons, A., and Courtier, P.: Les 25 ans du

717   système de prévision numérique du temps IFS/Arpège, La Météorologie, 89, 18–27,

718   https://doi.org/10.4267/2042/56594, 2015.

719   Ricaud, P., Gabard, B., Derrien, S., Chaboureau, J.-P., Rose, T., Mombauer, A. and Czekala,

720   H.: HAMSTRAD-Tropo, A 183-GHz Radiometer Dedicated to Sound Tropospheric Water

721   Vapor Over Concordia Station, Antarctica, IEEE T. Geosci. Remote, 48, 1365–1380, doi:

722   10.1109/TGRS.2009.2029345, 2010a.

723   Ricaud, P., Gabard, B., Derrien, S., Attié, J.-L., Rose, T., and Czekala, H.: Validation of

724   tropospheric water vapor as measured by the 183-GHz HAMSTRAD Radiometer over the

725   Pyrenees Mountains, France, IEEE T. Geosci. Remote, 48, 2189–2203, 2010b.

726   Ricaud, P., Genthon, C., Durand, P., Attié, J.-L., Carminati, F., Canut, G., Vanacker, J.-F.,

727   Moggio, L., Courcoux, Y., Pellegrini, A., and Rose, T.: Summer to Winter Diurnal

728   Variabilities of Temperature and Water Vapor in the lowermost troposphere as observed by

729   the HAMSTRAD Radiometer over Dome C, Antarctica, Bound.-Lay. Meteorol., 143, 227–

730   259, doi:10.1007/s10546-011-9673-6, 2012.

731   Ricaud, P., Grigioni, P., Zbinden, R., Attié, J.-L., Genoni, L., Galeandro, A., Moggio, A.,

732   Montaguti, S., Petenko, I., and Legovini, P.: Review of tropospheric temperature, absolute

humidity and integrated water vapour from the HAMSTRAD radiometer installed at Dome C, Antarctica, 2009–14, Antarct. Sci., 27, 598-616, doi:10.1017/S0954102015000334, 2015.

Ricaud, P., Bazile, E., del Guasta, M., Lanconelli, C., Grigioni, P., and Mahjoub, A.: Genesis of diamond dust, ice fog and thick cloud episodes observed and modelled above Dome C, Antarctica, Atmos. Chem. Phys., 17, 5221-5237, https://doi.org/10.5194/acp-17-5221-2017, 2017.

Ricaud, P., Del Guasta, M., Bazile, E., Azouz, N., Lupi, A., Durand, P., Attié, J.-L., Veron, D., Guidard, V., and Grigioni, P.: Supercooled liquid water cloud observed, analysed, and modelled at the top of the planetary boundary layer above Dome C, Antarctica, Atmos. Chem. Phys., 20, 4167–4191, https://doi.org/10.5194/acp-20-4167-2020, 2020.

Sippola, H., and Taskinen, P.: Activity of supercooled water on the ice curve and other thermodynamic properties of liquid water up to the boiling point at standard pressure, J. Chem. Engineer. Data, 63(8), 2986-2998, 2018.

Storelvmo, T. and Tan, I.: The Wegener–Bergeron–Findeisen process—Its discovery and vital importance for weather and climate, Meteor. Z, 24, 455-461, 2015.

Stull, R. B.: An introduction to boundary layer meteorology, Kluwer Academic Publisher, 1988.

Tomasi, C., Petkov, B., Mazzola, M., Ritter, C., di Sarra, A., di Iorio, T., and del Guasta, M.: Seasonal variations of the relative optical air mass function for background aerosol and thin cirrus clouds at Arctic and Antarctic sites, Remote Sensing, 7(6), 7157-7180, 2015.

Wegener, A. 1911. Thermodynamik der Atmosphäre. – Leipzig, Germany: Barth.

Wille, J. D., Favier, V., Dufour, A., Gorodetskaya, I. V., Turner, J., Agosta, C. and Codron, F.: West Antarctic surface melt triggered by atmospheric rivers, Nature Geoscience, 12(11), 911-916, 2019.

758 Young, G., Lachlan-Cope, T., O'Shea, S. J., Dearden, C., Listowski, C., Bower, K. N.,

759 Choularton, T. W., and Gallagher, M. W.: Radiative effects of secondary ice enhancement

760 in coastal Antarctic clouds, Geophys. Res. Lett., 46, 2312–2321,

761 https://doi.org/10.1029/2018GL080551, 2019.

762

763

Tables

764 **Table 1.** Time-coincident data availability (green) in Decembers 2018-2021 for HAMSTRAD

765 temperature and LWP, Lidar Backscattering and Depolarization and BSRN Surface Radiances

766 (Net, LWD, LWU, SWD and SWU). The 5 clear-sky (Reference) days are highlighted in red.

Year	December Days																														
	1	2	3	4	5	6	7	8	9	10	11	12	13	14	15	16	17	18	19	20	21	22	23	24	25	26	27	28	29	30	31
2018	🟩	🟥	🟩	🟩	🟩	🟩	🟩	🟩	🟩	🟩	🟩	🟩	🟩	🟩	🟩	🟩	🟩	🟩	🟥	🟩	🟩	🟩	🟩	🟩	🟩	🟩	🟩	🟩	🟩	🟩	🟩
2019	🟩	🟩	🟩	🟩	🟩	🟩	🟩	🟩	🟩	🟩	🟩	🟩	🟩	🟩	🟩	🟩															
2020				🟩	🟩	🟩	🟩	🟩	🟩	🟩	🟩	🟩	🟩	🟩	🟩	🟩	🟩	🟩	🟩	🟩	🟩		🟩	🟩	🟩	🟩	🟩	🟩	🟩	🟩	🟩
2021	🟩	🟩	🟥	🟩	🟩	🟩	🟩	🟩	🟩				🟩	🟩	🟩	🟩	🟥	🟩	🟩	🟩	🟩	🟩	🟩	🟩	🟩	🟥	🟩	🟩			🟩

767

768

769

770 **Table 2.** Gaussian functions fitted to the $N(x)$ function for $x = \theta$ (°C) or ΔSR (W m^{-2}). Units

771 of a_1, a_2, a_3, and c are in count number for θ and ΔSR; units of μ_1, μ_2, μ_3, σ_1, σ_2, and σ_3 are

772 in °C for θ and in W m^{-2} for ΔSR.

x	a_1	μ_1	σ_1	a_2	μ_2	σ_2	a_3	μ_3	σ_3	c
θ	15.0 10^3	-31.5	1.45	5.0 10^3	-28.0	1.65	0.5 10^3	-19.0	2.5	-9.1 10^{-6}
Net ΔSR	2106.5	0.02	19.2	941.4	29.8	22.0	-	-	-	19.5
LWD ΔSR	1010.8	80.1	21.9	1565.6	10.0	23.9	-	-	-	18.4
LWU ΔSR	1476.4	-10.0	14.9	1834.7	25.0	16.2	-	-	-	185.4
SWD ΔSR	1317.2	-5.0	15.8	717.4	-80.0	64.7	-	-	-	9.1
SWU ΔSR	1928.8	-5.0	19.2	1163.4	-59.9	17.6	-	-	-	9.1

773

774

Table 3. Coefficients of the relations $f(LWP) = a + b\ln(LWP)$ for the temperature θ or surface radiation anomalies ΔSR. Units of θ and ΔSR, as well as of their corresponding "a" values are in °C and W m^{-2}, respectively; units of b are in °C g^{-1} m^2 for θ and in W / g for ΔSR; units of LWP are in g m^{-2}. The last column shows the range of LWP values for which the relation is valid (in black), and in red (blue) the sub-range in which a positive (negative) impact is observed on ΔSR. Note that $a \pm \delta a$ corresponds to the range of a values where the relationship is valid.

$f(LWP)$	$a \pm \delta a$	b	Valid range for θ or ΔSR	Valid range for LWP
θ	-33.8 ± 1.5	6.5	$[-36; -16]$	$[1.0; 14.0]$
Net ΔSR	-50.0 ± 10.0	90.0	$[-15; 50]$	$[1.5; 3.0]$ / $[1.7; 3.0]$
LWD ΔSR	5.0 ± 15.0	65.0	$[-10; 100]$	$[0.8; 4.0]$ / $[1.0; 4.0]$
LWU ΔSR	-45.0 ± 30.0	90.0	$[-20; 40]$	$[1.3; 2.5]$ / $[1.6; 2.5]$
SWD ΔSR	30.0 ± 30.0	-130.0	$[-140; 10]$	$[1.1; 3.8]$ / $[1.2; 3.8]$
SWU ΔSR	15.0 ± 15.0	-75.0	$[-75; 10]$	$[1.1; 3.2]$ / $[1.2; 3.2]$
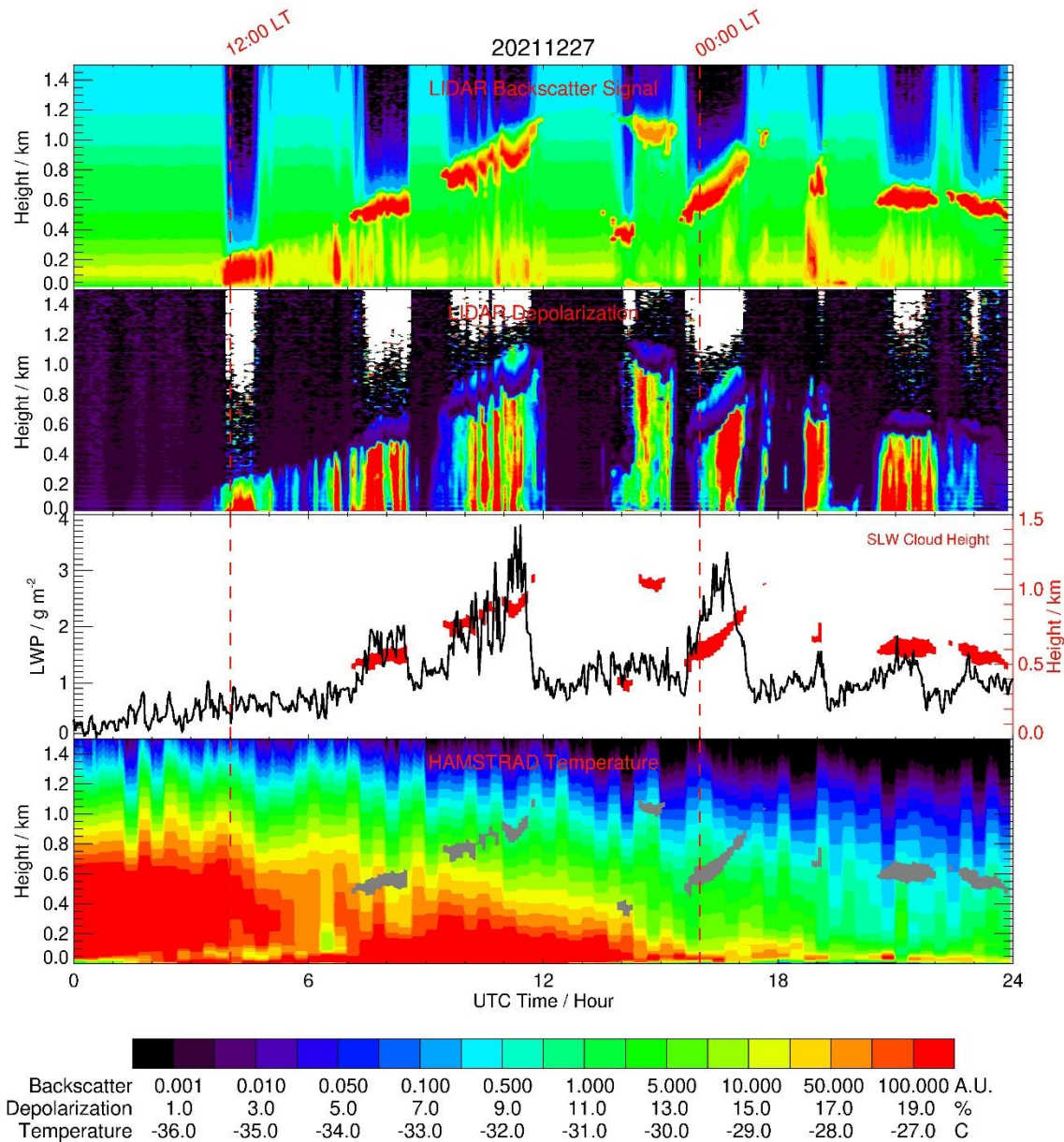
Figures

Figure 1: (From top to bottom): Time evolution (UTC, hour) of the Lidar Backscattering Signal, the Lidar Depolarization Signal, the HAMSTRAD LWP and the HAMSTRAD temperature profile measured on 27 December 2021. The time evolution of the SLW cloud (as diagnosed by a backscattering signal > 60 A.U. and a depolarization signal < 5%) is highlighted by the red and grey areas in the third and the forth panel from the top, respectively. The height above the ground is shown on the third panel from the top with the y-axis on the right. The 00:00 and 12:00 local times (LT) are highlighted by 2 vertical dashed lines.
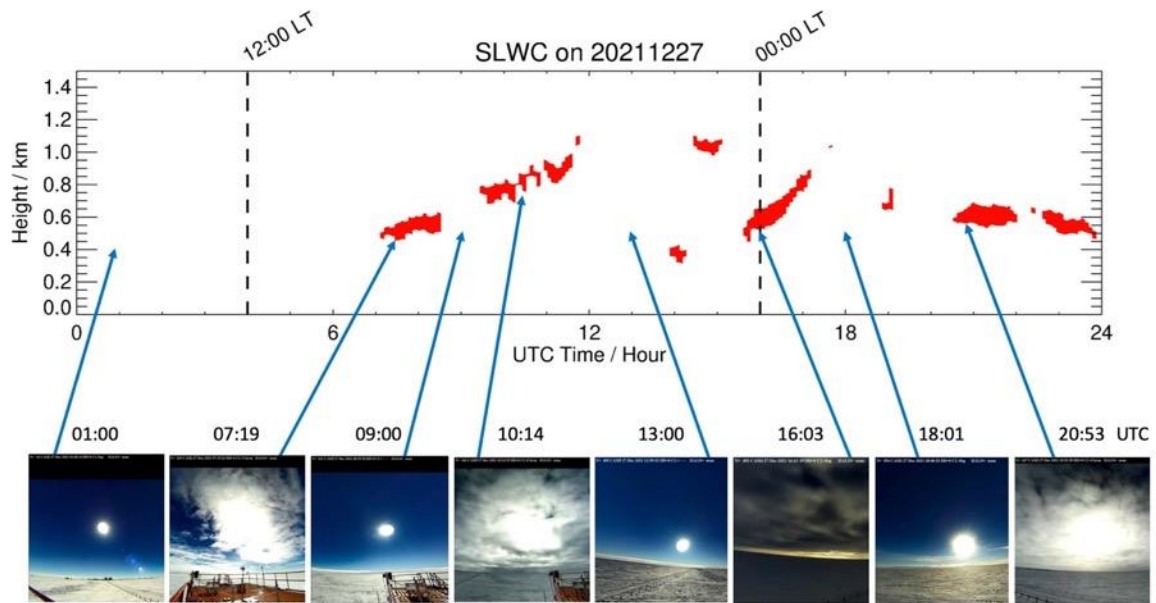
795

796 **Figure 2:** (Top) Time evolution (UTC, hour) of the SLWC (red areas) on 27 December 2021.

797 (Bottom, from left to right) Snapshots from the HALO-CAM video camera taken on: 01:00 (no

798 SLWC), 07:19 (SLWC), 09:00 (no SLWC), 10:14 (SLWC), 13:00 (no SLWC), 16:03 (SLWC),

799 18:01 (no SLWC) and 20:53 UTC (SLWC). The 00:00 and 12:00 local times (LT) are

800 highlighted by 2 vertical dashed lines.

801

802

803
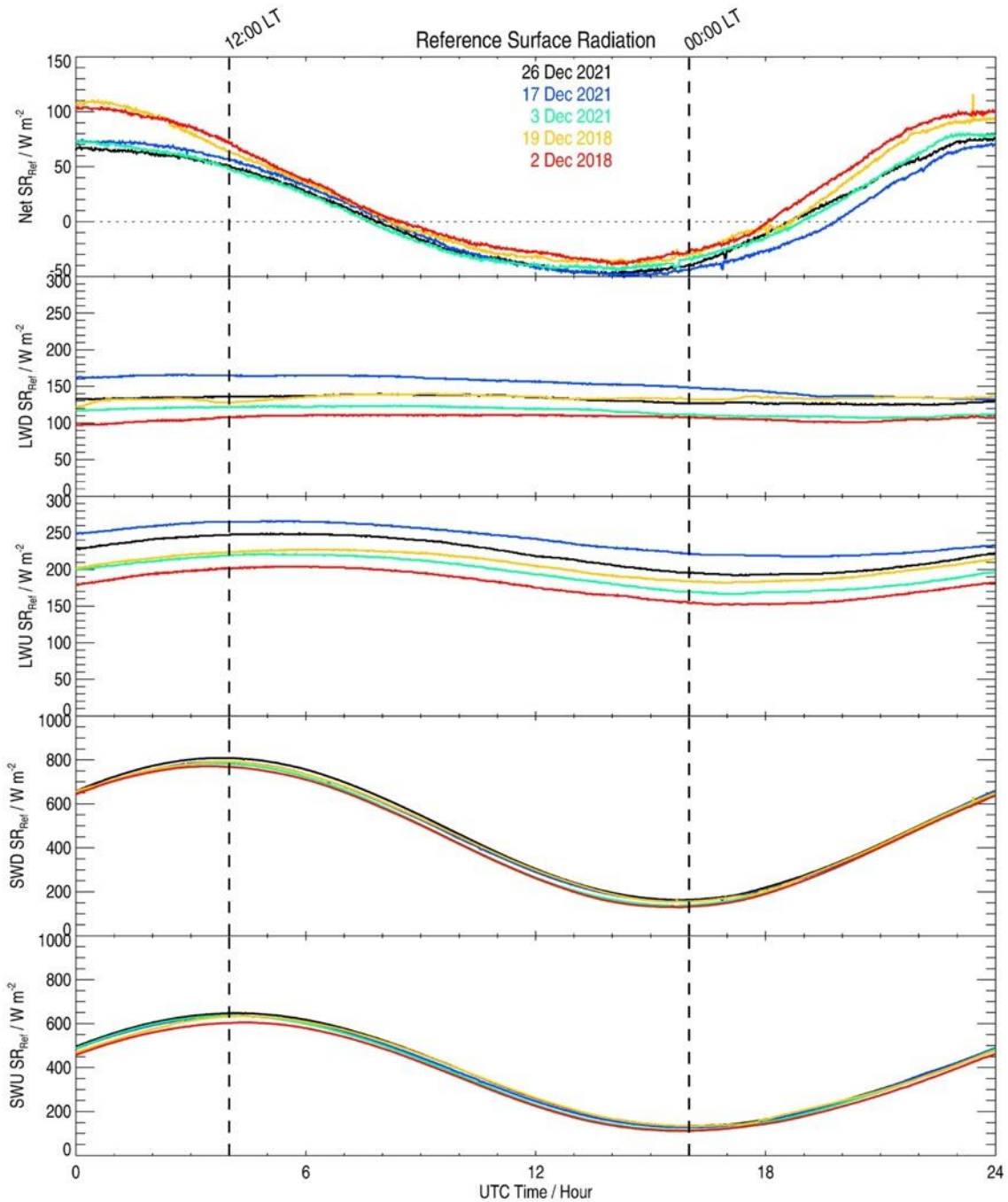
Figure 3: Time evolution (UTC, hour) of the clear-sky surface radiations (SR, W m^{-2}) observed

by the BSRN instruments on 2 December 2018 (red), 19 December 2018 (orange), 3 December

2021 (green), 17 December 2021 (blue) and 26 December 2021 (black): (from top to bottom)

Net SR, Longwave Downward SR (LWD SR), Longwave Upward SR (LWU SR), Shortwave

Downward SR (SWD SR) and Shortwave Upward SR (SWU SR). The 00:00 and 12:00 local

times (LT) are highlighted by 2 vertical dashed lines.

810
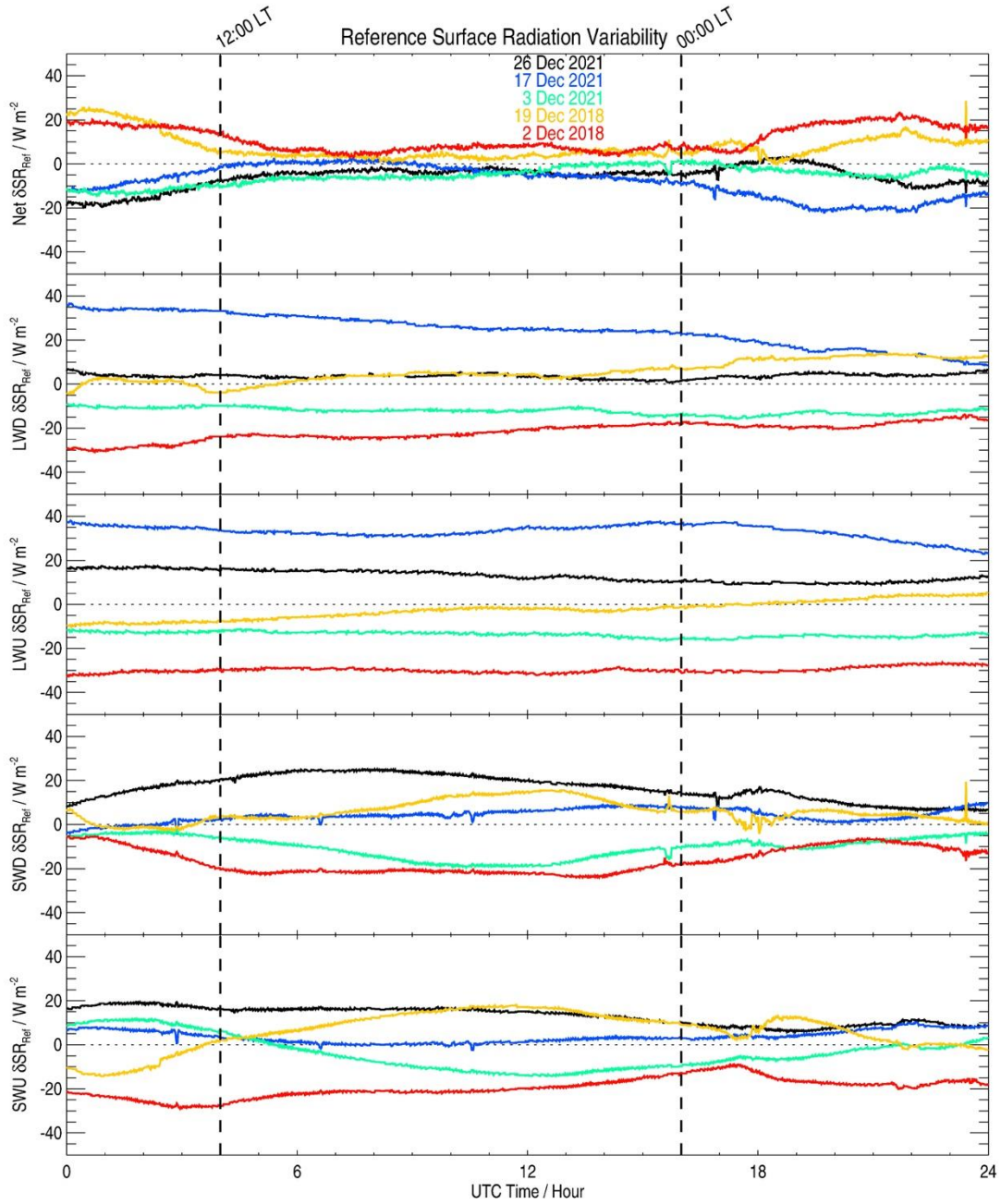
Figure 4: Time evolution (UTC, hour) of the clear-sky surface radiation variability (δSR_{Ref}, W

m^{-2}), namely the clear-sky surface radiations observed by the BSRN instruments on 2 December

2018 (red), 19 December 2018 (orange), 3 December 2021 (green), 17 December 2021 (blue)

and 26 December 2021 (black) minus the corresponding values averaged over the 5 cloud-free

days: (from top to bottom) Net SR, Longwave Downward SR (LWD SR), Longwave Upward

816   SR (LWU SR), Shortwave Downward SR (SWD SR) and Shortwave Upward SR (SWU SR).

817   The 00:00 and 12:00 local times (LT) are highlighted by 2 vertical dashed lines.

818

819

820
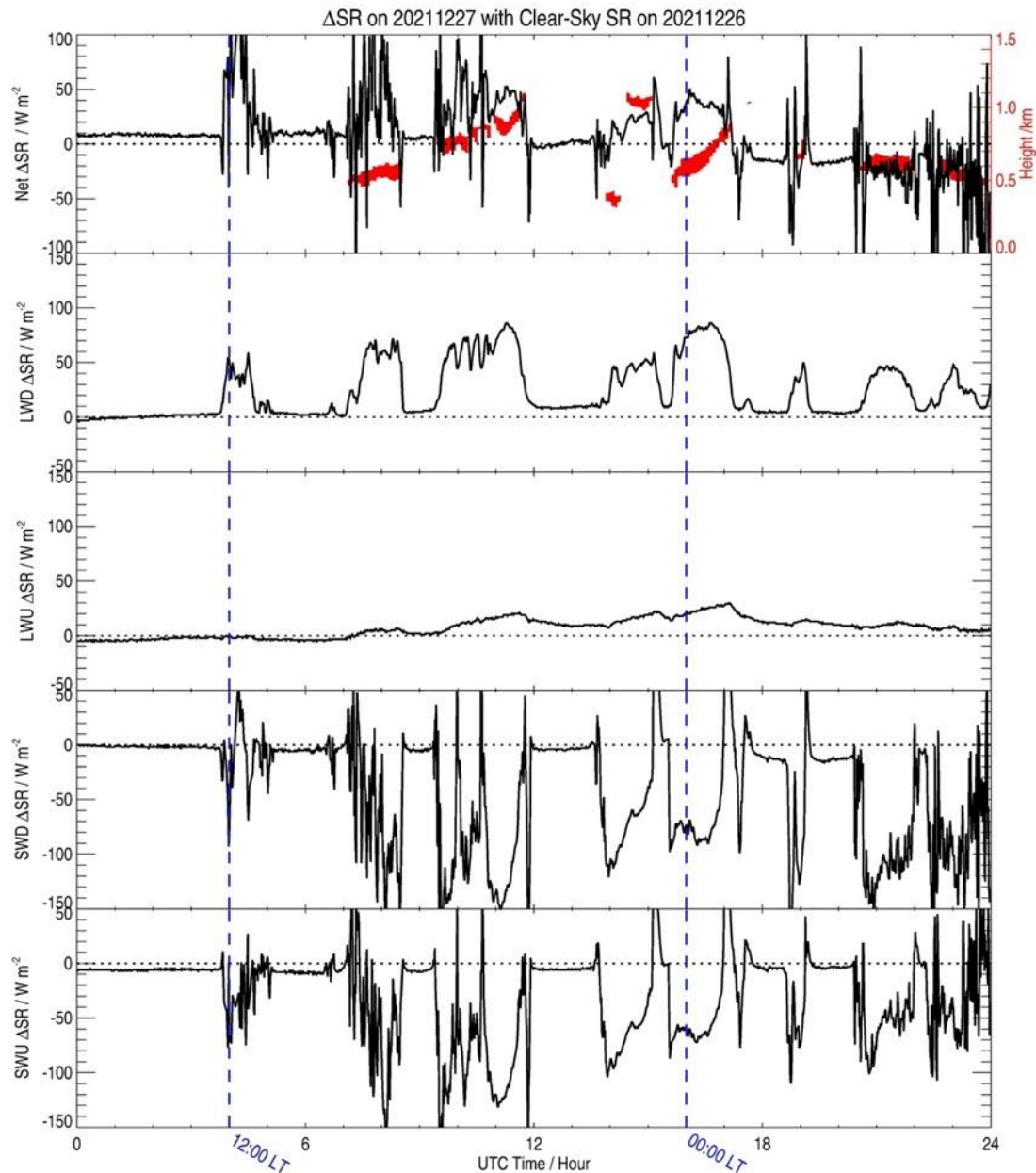
Figure 5: Time evolution (UTC, hour) of the Surface Radiation Anomaly (ΔSR), difference

between the SR (W m^{-2}) measured on 27 December 2021 and the reference clear-sky (SR_{Ref})

SR (W m^{-2}) measured on 26 December 2021: (from top to bottom) Net (Net ΔSR), longwave

downward (LWD ΔSR), longwave upward (LWU ΔSR), shortwave downward (SWD ΔSR) and

shortwave upward (SWU ΔSR). The time evolution of the SLW cloud is highlighted by a red

area in the uppermost panel, with the height on the y-axis shown on the right. The 00:00 and

12:00 local times (LT) are highlighted by 2 vertical blue dashed lines.

828
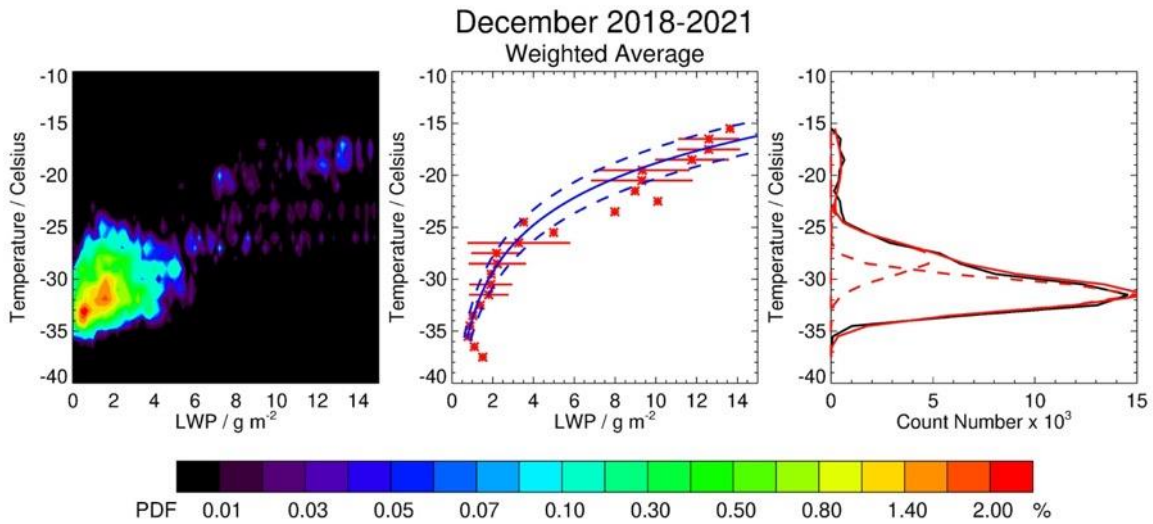
Figure 6: (Left) Probability Density (%) of the Temperature (°C) as a function of Liquid Water Path (LWP, g m^{-2}) contained in the Supercooled Liquid Water clouds (SLWCs) above Dome C in December 2018-2021. The Probability Density is defined in the text. (Centre) Weighted-average LWP vs. temperature (red asterisks) with a fitted logarithmic function (blue solid) encompassing the significant points (2 dashed blue lines). Horizontal bars represent 1-sigma variability in LWP per 1°C-wide bin over significant points. (Right) Temperature as a function of count number per 1°C-wide bin (black solid line) with 3 fitted Gaussian functions (red dashed curves). The sum of the 3 Gaussian functions is represented by a red solid line.

837

838

839
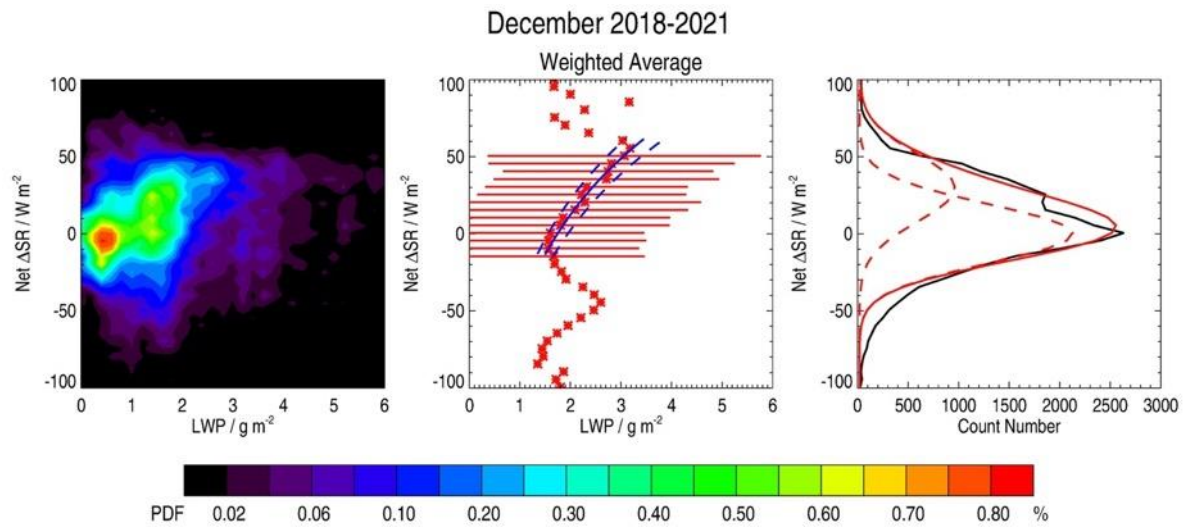
Figure 7: (Left) Probability Density (%) of the Net Surface Radiation Anomaly (Net ΔSR, W

m^{-2}) as a function of Liquid Water Path (LWP, g m^{-2}) contained in the Supercooled Liquid

Water clouds (SLWCs) above Dome C in December 2018-2021. The Probability Density is

defined in the text. (Centre) Weighted-average LWP vs. Net ΔSR (red asterisks) with a fitted

logarithmic function (blue solid) encompassing the significant points (2 dashed blue lines).

Horizontal bars represent 1-sigma variability in LWP per 5 W m^{-2}-wide bin over significant

points. (Right) Net ΔSR as a function of count number per 5 W m^{-2}-wide bin (black solid line)

with 2 fitted Gaussian functions (red dashed curves). The sum of the 2 Gaussian functions is

represented by a red solid line.

849
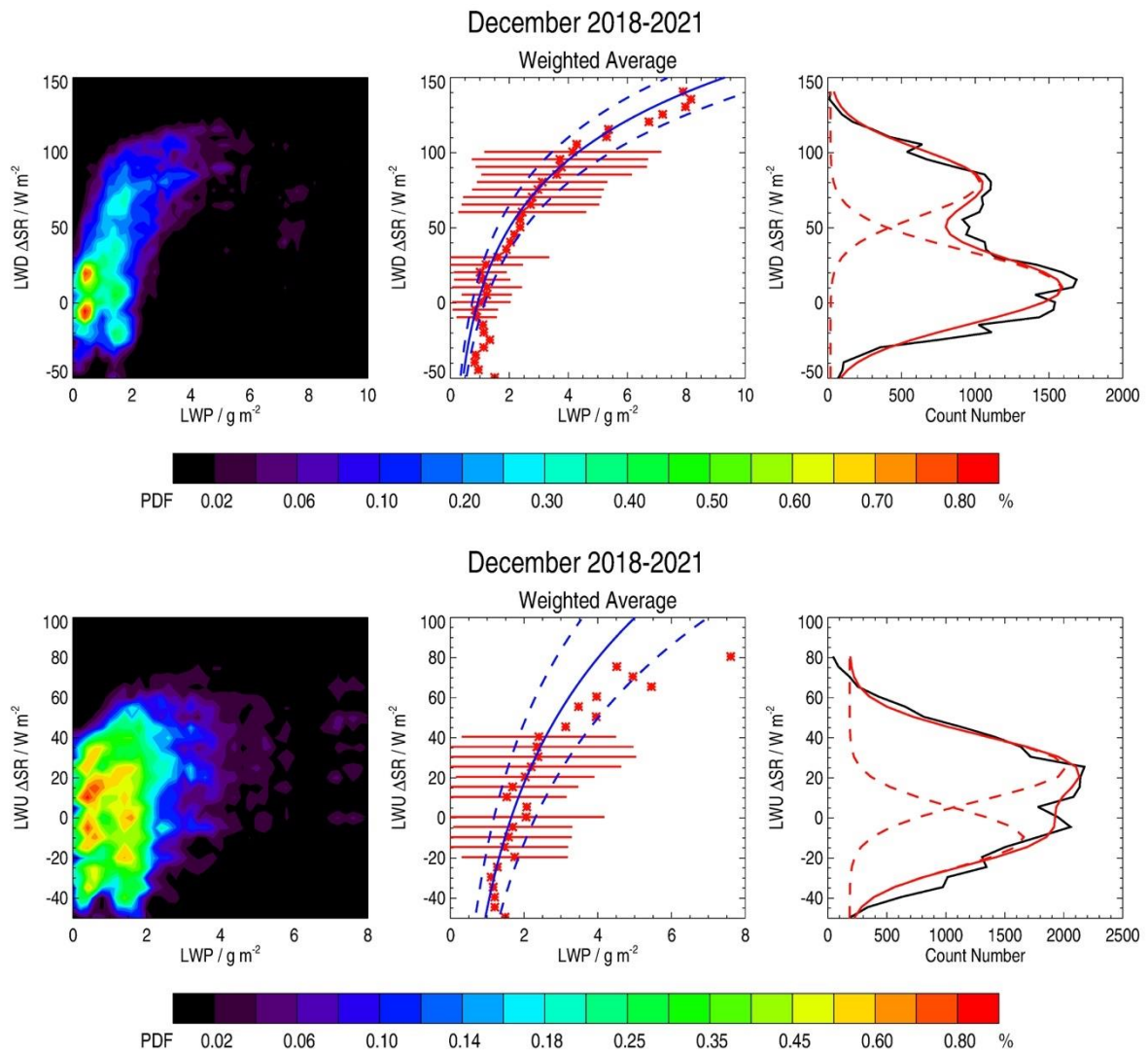
850

851 **Figure 8:** As in Figure 7 but for the Longwave Downward (top) and Upward (bottom) Surface

852 Radiation Anomaly (LWD and LWU ΔSR, respectively).

853

854

855
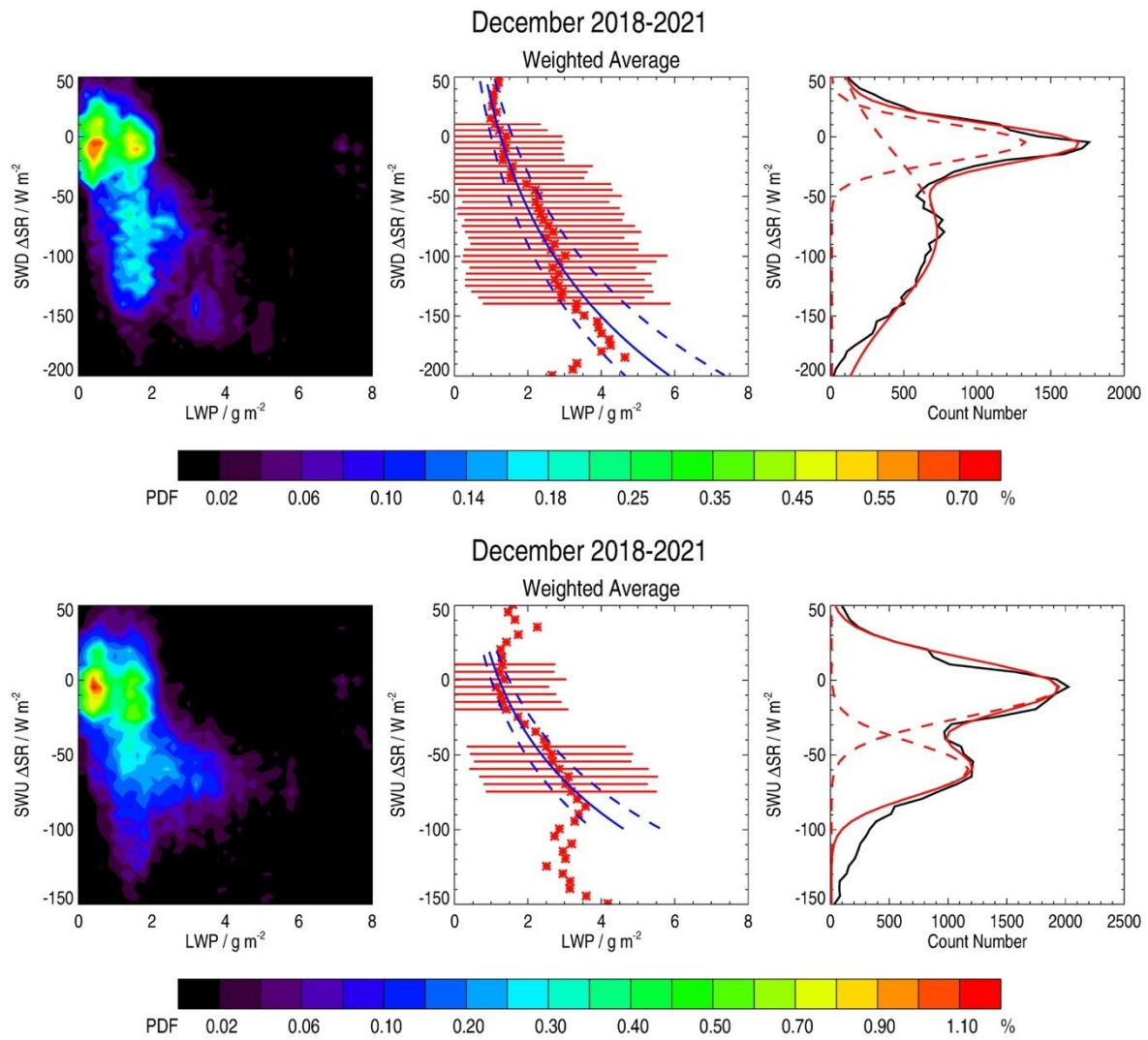
Figure 9: As in Figure 7 but for the Shortwave Downward (top) and Upward (bottom) Surface

Radiation Anomaly (SWD and SWU ΔSR, respectively).

858

859

860
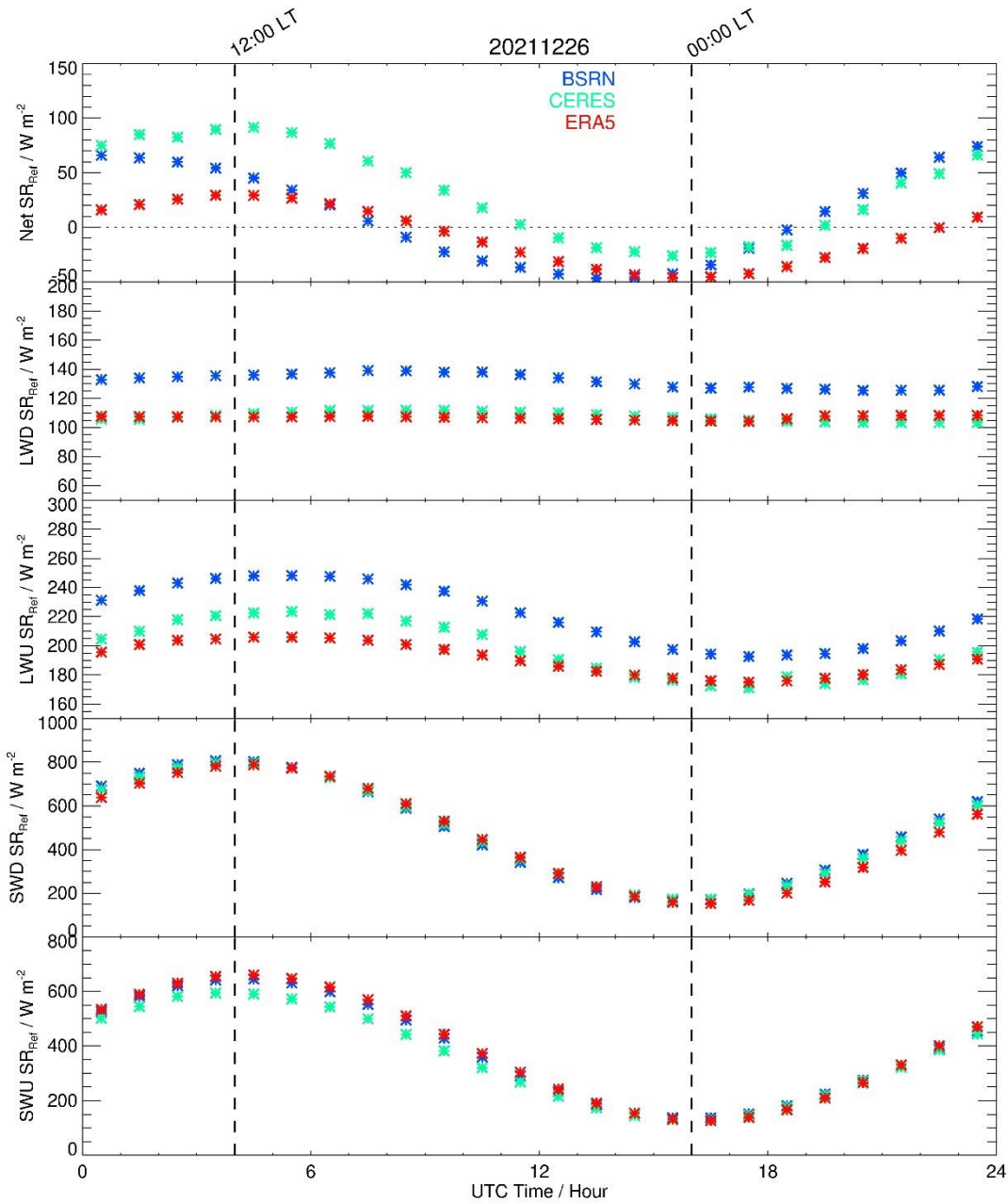
Figure 10: Hourly time evolution (UTC, hour) of the clear-sky surface radiations (SR, W m^{-2})

862 observed by the BSRN instruments (blue asterisks), the CERES (green asterisks) and the ERA5

863 (red asterisks) data sets on 26 December 2021: (from top to bottom) Net SR, Longwave

864 Downward SR (LWD SR), Longwave Upward SR (LWU SR), Shortwave Downward SR

865 (SWD SR) and Shortwave Upward SR (SWU SR). The 00:00 and 12:00 local times (LT) are

866 highlighted by 2 vertical dashed lines.

867
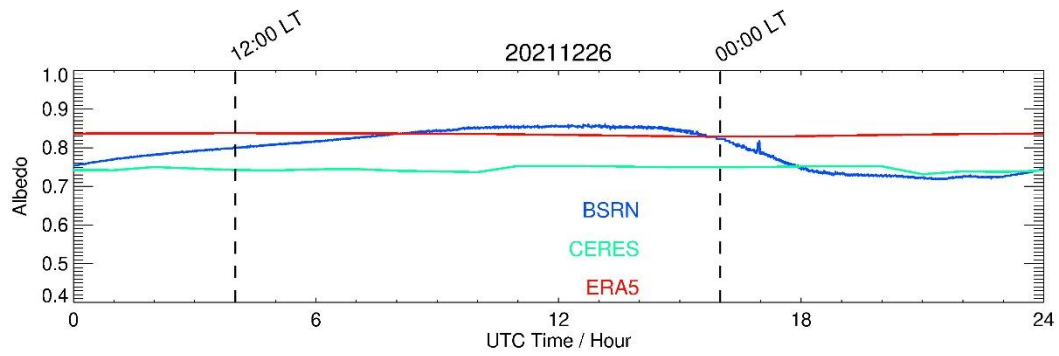
Figure 11: Time evolution (UTC, hour) of the surface albedo observed by the BSRN instruments (blue), the CERES (green) and the ERA5 (red) data sets on 26 December 2021. The 00:00 and 12:00 local times (LT) are highlighted by 2 vertical dashed lines.

Figure 12: Image of the sastrugi on the ice surface (Wikimedia Commons).
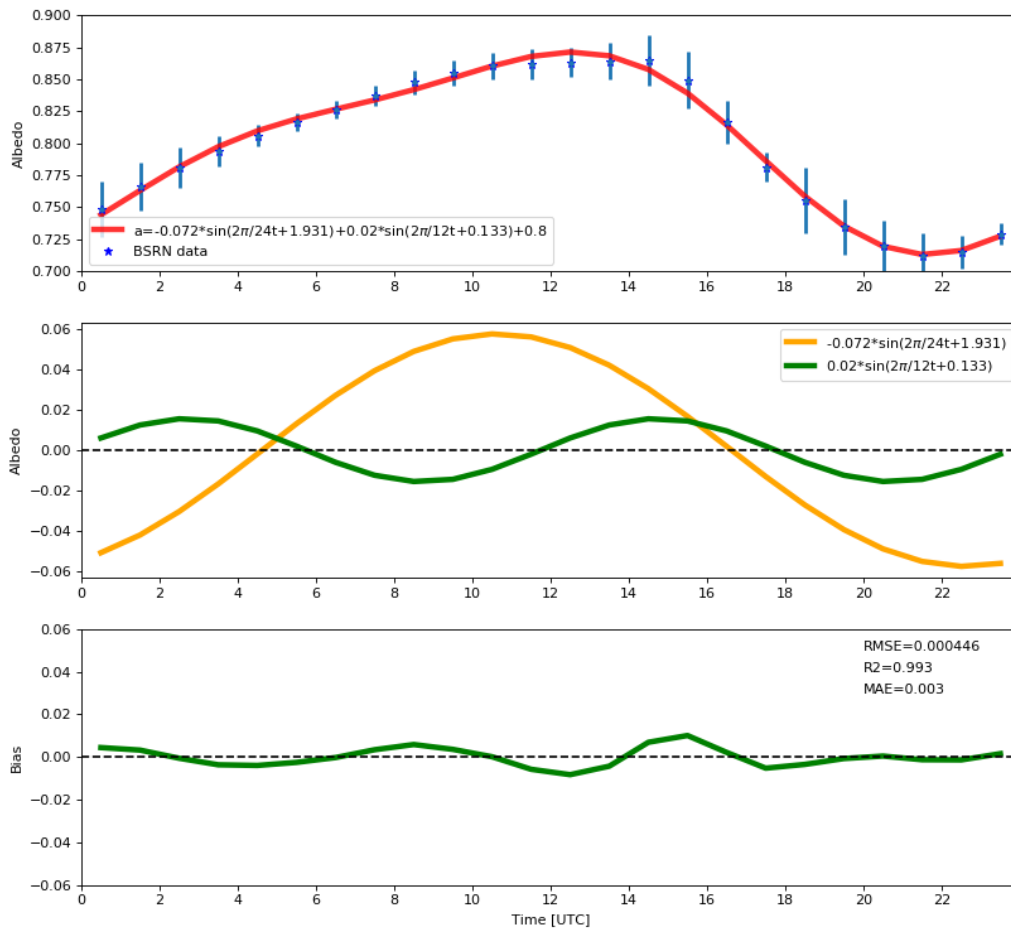
Figure 13: (Top) Hourly time evolution (UTC, hour) of the mean surface albedo observed by the BSRN instruments (blue star) associated with the 5 clear-sky periods under consideration in our analysis together with the associated standard deviation (vertical bar) together with the fitted trigonometric function based on 2 sine functions (red). (Center) The 2 sine functions fitting the hourly time evolution of the BSRN mean surface albedo. (Bottom) Hourly time evolution (UTC, hour) of the albedo residuals (BSRN-fit) and associated Root Mean Square Error (RMSE), Coefficient of determination (R^2), and Mean Absolute Error (MAE).

885
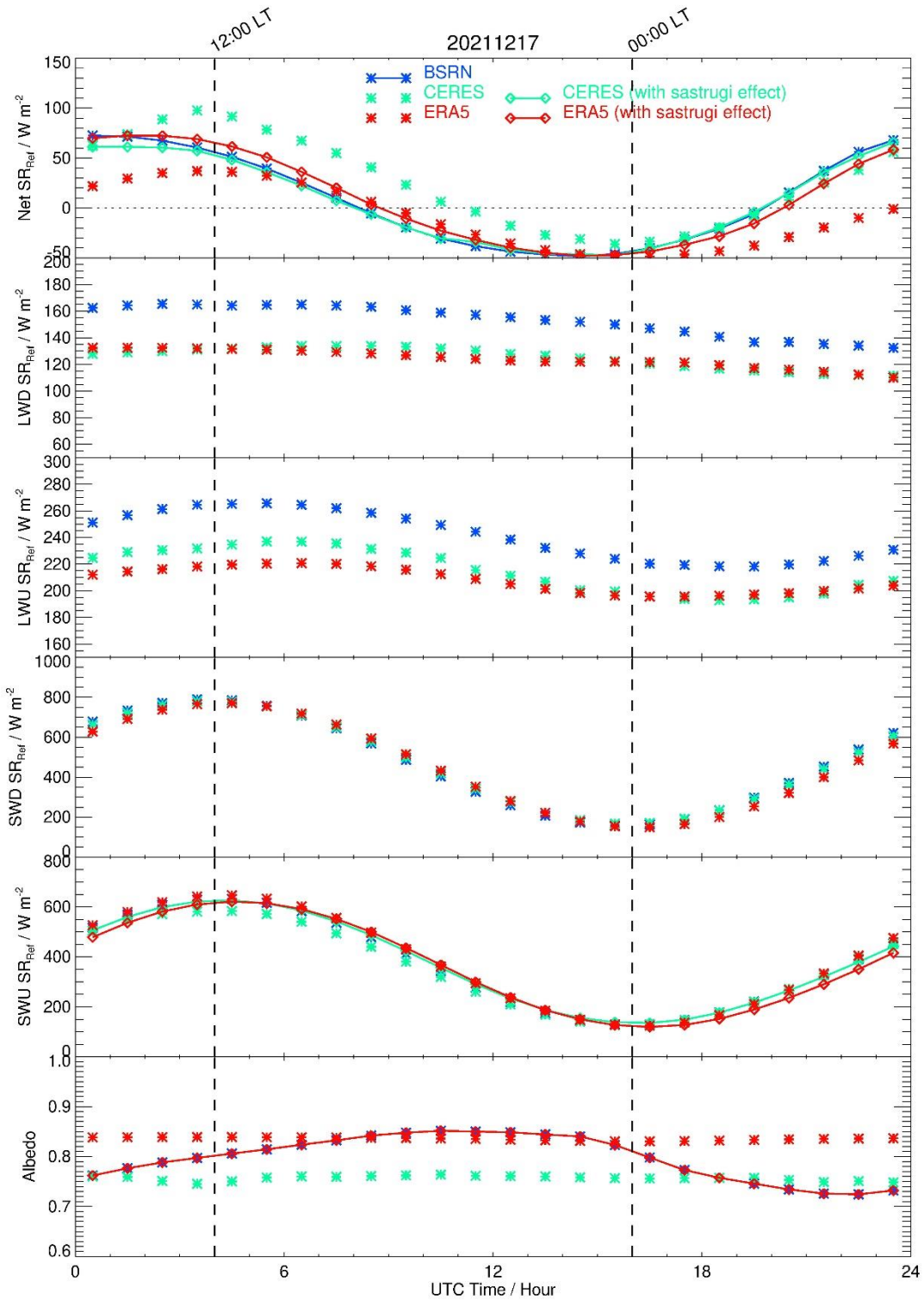
Figure 14: Same as Figure 11 with the albedo inserted in the lowermost panel. Net SR, SWU

SR, and albedo including the sastrugi effect for ERA5 (red solid line) and CERES (green solid

line) have also been added in the Figures.

889

890
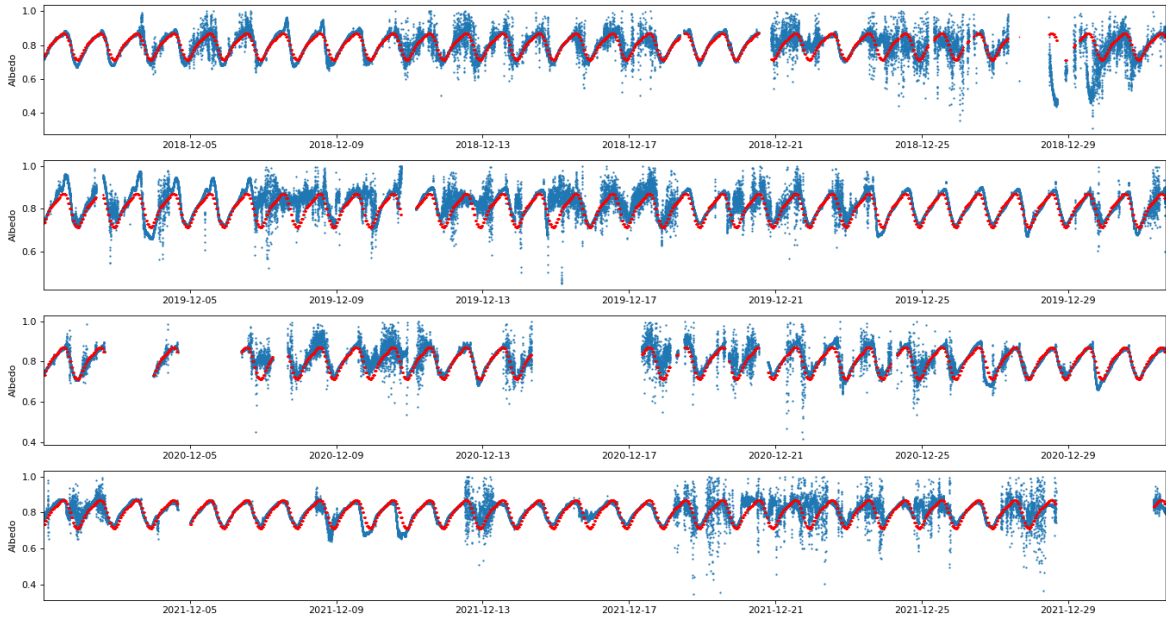
Figure 15: Hourly time evolution (UTC, hour) of the surface albedo observed by the BSRN

instruments (blue), and using the fit function based on 2 sine functions (red) for the whole

BSRN data set covering the month of December in 2018, 2019, 2020 and 2021.

894